UC Santa Barbara

UC Santa Barbara Previously Published Works

Title

Phase Stability and Diffusion in Lateral Heterostructures of Methyl Ammonium Lead Halide Perovskites

Permalink

Journal

ISSN

Authors

Kennard, Rhys M
Dahlman, Clayton J
Nakayama, Hidenori
et al.

Publication Date

DOI

Peer reviewed

Phase Stability and Diffusion in Lateral Heterostructures of Methyl Ammonium Lead Halide Perovskites

Rhys M. Kennard, [†] Clayton J. Dahlman, [†] Hidenori Nakayama, [†§] Ryan A. DeCrescent, [§] Jon A. Schuller, [‖] Ram Seshadri, [†‡] Kunal Mukherjee, [†] Michael L. Chabinyc [†*]

† Materials Department, University of California, Santa Barbara, California 93106, United States

§Electronics Materials and New Energy Laboratory, Mitsubishi Chemical Corporation, Yokohama R&D Center 1000, Kamoshida-cho, Aoba-ku, Yokohama 227-8502, Japan

§ Department of Physics, University of California, Santa Barbara, California 93106, United States

‖ Department of Electrical and Computer Engineering, University of California, Santa Barbara, California 93106, United States

‡ Department of Chemistry & Biochemistry, University of California Santa Barbara, Santa Barbara, CA 93106-9510

Corresponding Author
*Email: mchabinyc@engineering.ucsb.edu

ABSTRACT. Mixed-halide hybrid organic inorganic perovskites have band gaps that span the visible spectrum making them candidates for optoelectronic devices. Diffusion of the halide atoms in methyl ammonium lead iodide (MAPbI$_3$) and its alloys with bromine has been observed in both dark and under illumination. While halide transport upon application of electric fields has received much attention, less is known regarding bromide and iodide interdiffusion down concentration gradients. This work provides an upper bound on the bromide-iodide interdiffusion coefficient D_i, in thin films of (MAPbBr$_x$I$_{1-x}$)$_3$ using a diffusion couple of a lateral heterostructure. The upper bound of D_i was extracted from changes in the interface profiles of the heterostructures upon exposure to heat. The stability of thoroughly-heated interfacial profiles suggests that the miscibility gap extends to higher temperatures and to a higher fractional composition of bromine than predicted by theory. The results of this work provide guidance for compositions of thermally stable heterostructures of hybrid halide perovskites.

INTRODUCTION

Hybrid halide perovskites have recently emerged as candidates for optoelectronic applications because they exhibit solar cell efficiencies similar to those of crystalline silicon,[1,2] are solution processable, and are made from inexpensive, earth-abundant materials.[3–6] Hybrid halide perovskites have an ABX_3 structure, where A is a cation (e.g. Cs^+, $CH_3NH_3^+$, $CH_5N_2^+$), B is a metal (e.g. Pb, Sn, Bi) and X is a halide. Mixed A-site cations and halides can be used to tune the optical gap and structure near room temperature; the resulting alloys have the highest power conversion efficiency in solar cells.[1,7–14] Films of nanocrystals of alloys are efficient light emitters, with quantum yields up to 90 %,[15] and have been explored for LED applications.[16] Despite the successes of alloys, halides can diffuse in hybrid perovskites, [17] which negatively impacts the performance of devices. Hysteresis in the current-voltage characteristics of solar cells is attributed to halide migration.[18,19] Mixed bromide-iodide perovskites can phase separate into I-rich and Br-rich domains upon light exposure,[20-31] leading to instabilities in the performance of Br-rich perovskite solar cells.[32-37] A thorough understanding of halide movement in mixed-halide perovskites is therefore desirable for future design of efficient devices.

While much progress has been made towards understanding the mechanisms and kinetics of light-induced phase separation,[20-31] the diffusion of halides in $MAPb(Br_xI_{1-x})_3$ without illumination is not as well understood. Many studies have focused on ion/vacancy movement in response to an electric field,[18,38-48] rather than on ion/vacancy movement down a concentration gradient.[29,49] Recent work has elucidated interdiffusion behavior of bromide and chloride in $CsPb(Br_xCl_{1-x})_3$ nanowires;[49,50] however, interdiffusion in Br-I systems has been less explored. Halide interdiffusion constants were previously extracted from $CsPbBr_3$-$MAPbI_3$ [49] and $PbBr_2$-$MAPbI_3$ [29] heterostructures, where distances travelled by the halides in a given time enabled calculation of

the diffusion constant.[29,49] However, halide interdiffusion in $CsPbBr_3$-$MAPbI_3$ and $PbBr_2$-$MAPbI_3$ may differ from that in pure $MAPbX_3$ because of differences between the phase diagrams of the systems. Studies of Br-I interdiffusion in the $MAPb(Br_xI_{1-x})_3$ system are further complicated by the prediction of a miscibility gap,[51-52] where compositions within the gap phase-separate into I-rich and Br-rich regions, impeding halide interdiffusion down concentration gradients.

Here, we examine interdiffusion of halides in diffusion couples with varying composition of $MAPb(Br_xI_{1-x})_3$ at temperatures relevant to electronic devices. Using a halide substitution procedure, we fabricated lateral heterostructures of hybrid halide perovskite thin films and examined changes in the interfacial profiles upon exposure to heat and light. The stability of interfacial profiles confirmed that the interdiffusion coefficients D_i at temperatures relevant to device operation are low, and suggests that the $MAPb(Br_xI_{1-x})_3$ miscibility gap extends to higher temperatures and more Br-rich compositions than expected based on computational models. These results suggest compositions where it is possible to form heat-stable heterostructures of $MAPb(Br_xI_{1-x})_3$.

RESULTS AND DISCUSSION
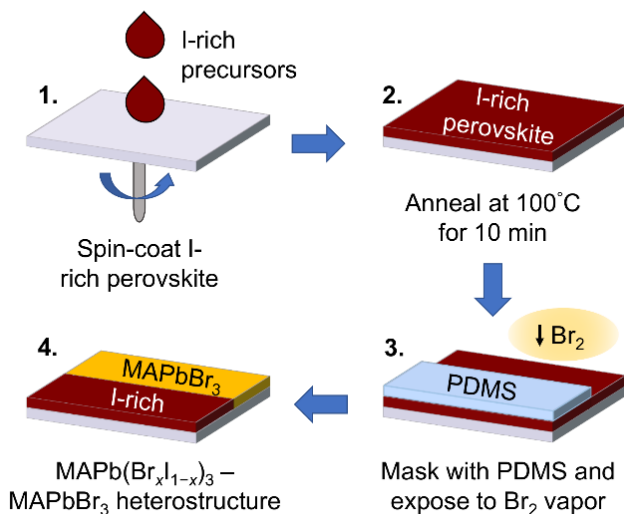
Figure 1. Fabrication procedure for perovskite-perovskite heterostructures.

To fabricate a diffusion couple comprising a lateral heterostructure of two compositions of MAPb(Br$_x$I$_{1-x}$)$_3$, we used a two-step process. First, we spin-coated an I-rich perovskite thin film and then we used a halide exchange reaction to form the heterostructure.[53] We sought a methodology that would reflect the crystallinity and microstructure of thin films typically used in devices. Other heterostructures or halide gradients have been formed by processes including solution exchange,[54] placement of microplates on top of nanowires,[49] activation of phase separation/domain merging in single crystal nanowires using light,[25] electron-beam lithographic patterning of nanowires,[55] and contacting nanowires with single crystals.[56] While lithographic patterning enables fabrication of very sharp patterns, developers and electron beams may cause sample damage and/or introduce vacancies in the hybrid halide perovskites.[57] Modification of the halide composition using precursors in solvent may also impact the crystallinity of the substituted layer due to recrystallization. We therefore selected substitution by reaction with a vapor of Br$_2$ to ensure that the I-rich and Br-rich perovskites had similar morphology and grain size,[53] which is

desirable for interdiffusion studies. As with many substitution procedures, the number of vacancies in the Br_2-exposed side may change relative to that on the masked side, which could change the rates of interdiffusion in these two areas relative to other methods.

The procedure to form lateral heterostructures is shown in **Figure 1**. Iodine-rich perovskites were spin-coated onto quartz substrates. We chose an I-rich perovskite spin-coating procedure that yields 17% solar cell efficiency for $MAPbI_3$, before any halide substitution (**Figure S1**). A ≈ 450 μm-thick PDMS conformal mask was then laid on top of the thin film of $MAPb(Br_xI_{1-x})_3$, thus covering half of the 1.5 cm × 1.5 cm × 300 nm thin film. The masked film was exposed to bromine vapor (≈ 0.48 atm) in a nitrogen environment. The PDMS acted as a barrier to the bromine vapor and the exposed areas were allowed to react fully with the vapor, yielding $MAPbBr_3$. Consistent with previous reports,[53] the reaction was complete within one minute, indicating rapid reaction of Br_2 with $MAPbI_3$. The PDMS was then peeled off, leaving behind a lateral heterostructure of $MAPb(Br_xI_{1-x})_3|MAPbBr_3$. We focused on heterostructures with three compositions: $MAPbI_3|MAPbBr_3$, $MAPb(Br_{0.12}I_{0.88})_3|MAPbBr_3$, and $MAPb(Br_{0.70}I_{0.30})_3|MAPbBr_3$. These are hereafter referred to as $x_{Br} = 0|1$, $x_{Br} = 0.12|1$, and $x_{Br} = 0.70|1$ heterostructures respectively. We chose to examine the response of iodine-containing phases $x_{Br} = 0.12$ and $x_{Br} = 0.70$, in addition to that of $x_{Br} = 0$, because these are at the approximate locations of the binodal lines at room-temperature predicted by calculations using density functional theory.[51]
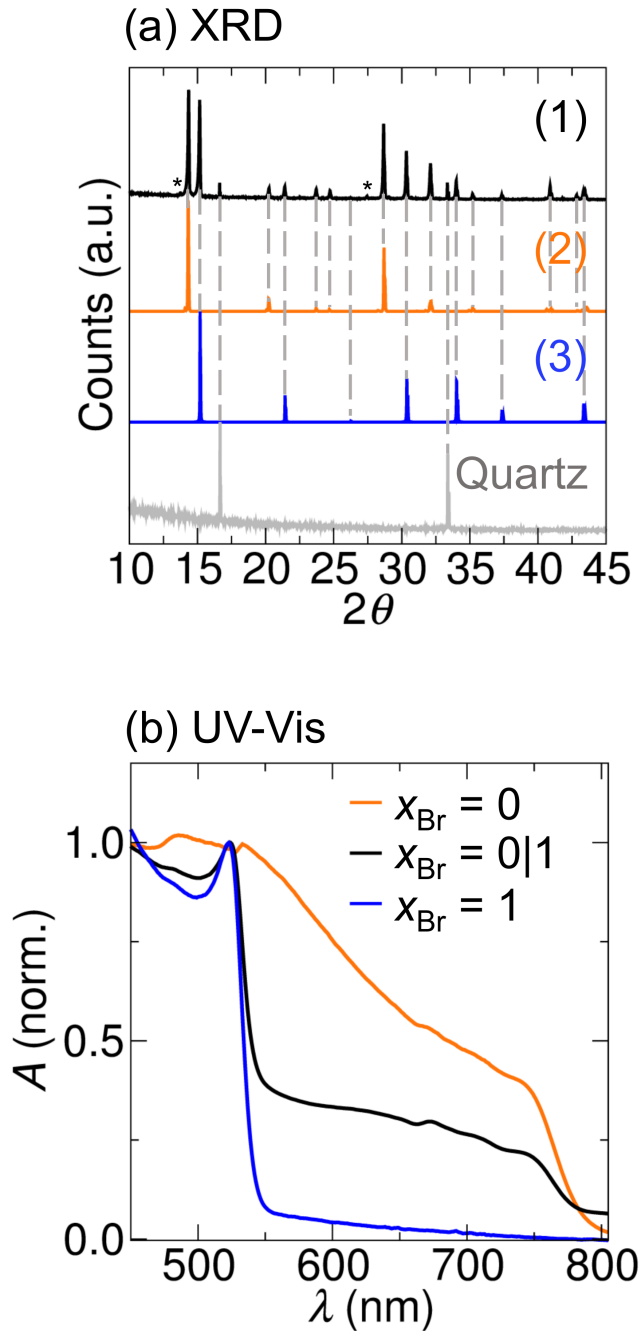
Figure 2. (a) XRD patterns of the MAPbI$_3$-MAPbBr$_3$ heterostructure (x_{Br} = 0|1 - black trace (1)), of simulated MAPbI$_3$ (orange trace (2)), of simulated MAPbBr$_3$ (blue trace (3)), and the quartz substrate (gray trace). Simulations were performed using the *I4/mcm* structure of MAPbI$_3$ [58] and using the *Pm-3m* structure of MAPbBr$_3$.[26] The dotted gray lines are guides for the eye, and the black * indicate additional peaks arising from Tungsten (1.4764 Å) and CuKβ (1.3926 Å) contamination in the X-Ray source. (b) UV-Vis spectra of the MAPbI$_3$-MAPbBr$_3$ heterostructure, of spin-cast MAPbI$_3$ and of spin-cast MAPbBr$_3$.

The conformal mask and substitution by Br_2 vapor led to complete exchange of the halide along with an interfacial region (70 - 100 microns wide) of mixed composition; examination of changes along this interfacial region in response to heat was used to analyze phase behavior in $MAPb(Br_xI_{1-x})_3$, as will be discussed later. Formation of the desired heterostructures was confirmed via X-Ray Diffraction (XRD), UV-Vis spectroscopy (**Figure 2**), Scanning Electron Microscopy (SEM – **Figure 3**) combined with Energy-Dispersive X-ray analysis (EDX – **Figures S2, S3 and S4**) and confocal microscopy (**Figures 3** and **S5**). XRD of the entire film of an x_{Br} = 0|1 heterostructure displayed peaks corresponding to both $MAPbI_3$ and $MAPbBr_3$, indicating full replacement of the iodine with bromine (**Figure 2a**). Similarly, the UV-Vis spectrum of an x_{Br} = 0|1 heterostructure displayed increased absorption at the onsets of the $MAPbI_3$ and $MAPbBr_3$ bandgaps (**Figure 2b**). XRD and UV-Vis characterization for the x_{Br} = 0.12|1 and x_{Br} = 0.70|1 heterostructures also confirmed formation of the desired phases (**Figure S6**). Plan view SEM of x_{Br} = 0|1 revealed the local structure of the interfacial region (**Figure 3a**). The films comprised ≈ 300 nm grains contained in large, continuous domains, which is favorable for examining halide diffusion across large areas. The change in contrast in domains along the interface indicated that halide substation occurred in the middle of the domains (**Figure 3a**). Top-view and cross-sectional EDX (**Figures 4**, **S2, S3, and S4**) confirmed the locations of Br and I, and thus of x_{Br} = 0 and x_{Br} = 1. No iodine was observed above noise level in the x_{Br} = 1 region, again suggesting complete removal of iodine from this area. Intermediate x_{Br} compositions along the interface were assigned based on halide content relative to the EDX- and optically-determined x_{Br} = 0 and x_{Br} = 1 compositions for x_{Br} = 0|1. Similar analysis was performed to determine macroscopic interfacial composition in the x_{Br} = 0.12|1 and x_{Br} = 0.70|1 heterostructures. EDX baseline compositions were obtained far from the interface (data not shown) to confirm lack of bromine in x_{Br} = 0 and lack of

iodine in $x_{Br} = 1$ (**Figures 4, 6** and **S3**). The interface width was determined to be ≈100 μm (**Figures 4** and **S3**) via both EDX, optical microscopy, and confocal laser scanning microscopy (**Figures 3b-d** and **S5**). We attribute the width of the interfacial region to our fabrication procedure in which Br_2 vapor permeates PDMS at the edge of the mask (**Figure S7**); and note that in a system with a miscibility gap, which is predicted for the $MAPb(Br_xI_{1-x})_3$ system,[51] a sharp interface would be expected with an impermeable mask.
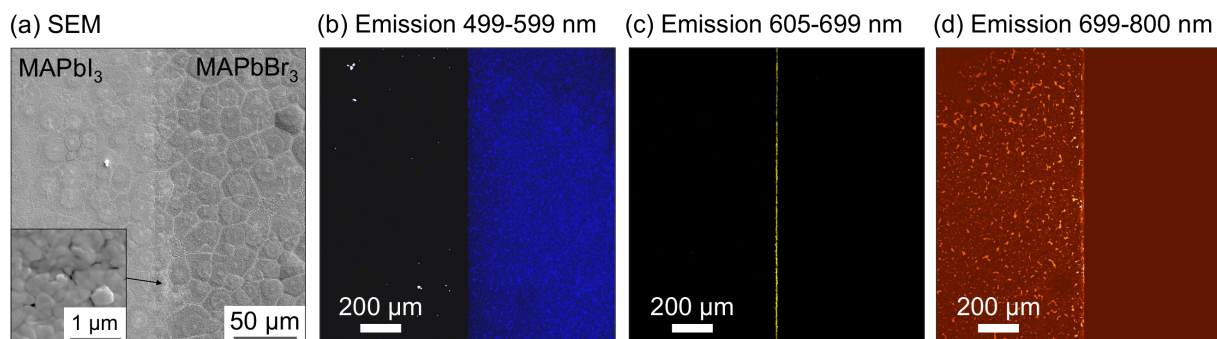
Figure 3. Plan view SEM of an MAPbI3-MAPbBr₃ heterostructure before heating (a). The inset in is a high-magnification view of the area indicated by the arrow. Confocal scanning luminescence emission map at three windows of emission, 499 - 599 nm (b), 605 - 699 nm (c), and 699 - 800 nm(d), each labelled with false color, of an MAPbI₃-MAPbBr₃ heterostructure before heating, with excitation wavelength 458 nm.

We examined the phase stability of the heterostructures upon heating without light exposure, at temperatures relevant for thin film devices (see **Methods section in the SI**). Operating temperatures are typically under 70°C for solar cells[59] and lamination or curing temperatures for solar cell encapsulants can exceed 100°C.[60,61] The miscibility gap for $MAPb(Br_xI_{1-x})_3$ calculated by DFT extends to 70°C,[51] leading to the expectation that halides will not diffuse down concentration gradients below this temperature. We therefore selected 100°C because it is within the window of temperatures encountered under practical conditions for devices and can test the

expected miscibility of the halide ions, at a temperature that will not be too damaging to the perovskite layer.[62] Prior to heating, we spin-coated a thin layer of polystyrene on top of the heterostructure, both to prevent desorption of methylammonium, enabling lengthy and high-temperature experiments, and to minimize diffusion along the perovskite surface. The heterostructures were heated for extended times (up to 360 min.) on a hot plate with a heat diffuser in a nitrogen-filled glove box. Lack of degradation and changes in grain structure after heating were confirmed via XRD and top-view SEM (**Figures S8 and S9**). The heat diffuser was encased in aluminum foil to ensure that the samples were kept in the dark, as light may affect halide transport. After heating, the compositional profiles at the heterostructure interface were analyzed via optical microscopy in transmission mode and via EDX (**Figure 4**). At each time point, the samples were quickly removed from the hot plate/heat diffuser in the glove box for optical microscopy analysis and were placed again on the heat diffuser afterwards. The total time off of the hot plate, at each time point, was kept under 10 min. This method ensured rapid quenching of any halide migration, which would be visible via change in local bandgap. Using optical microscopy to obtain interface profiles enabled repeated analysis of the same location on each heterostructure at each time point, enabling very rapid analysis of the interface profiles at specific times. Optical microscopy also circumvented potential electron beam-induced sample damage (and corresponding changes in vacancy concentration) that may have occurred during EDX analysis. Interface profiles were subsequently analyzed after heating via EDX to confirm the composition.
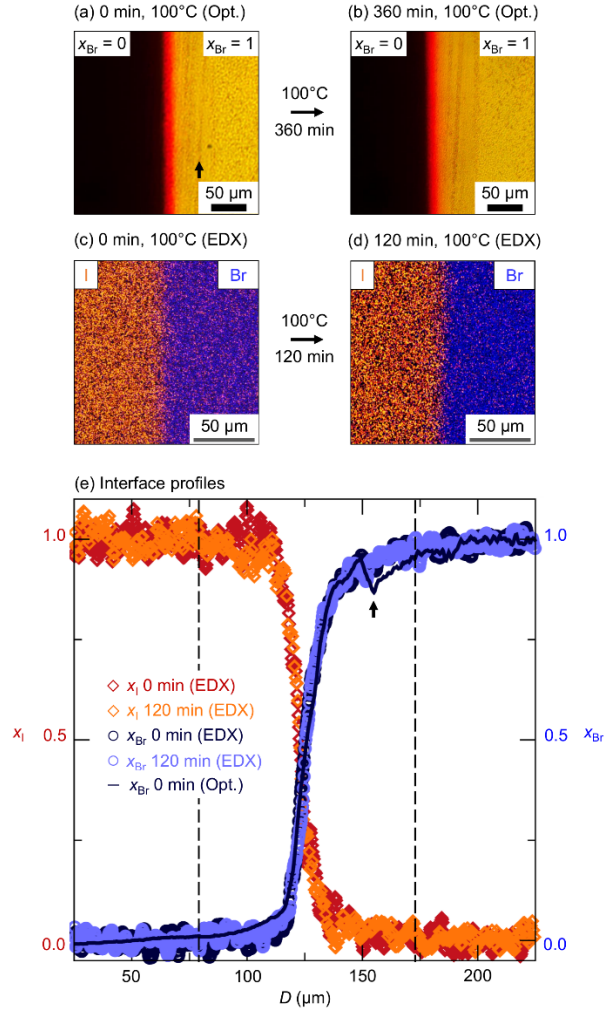
Figure 4. Optical microscopy images (transmission mode) of the same x_{Br} =0|1 heterostructure before (a) and after (b) heating at 100°C for 360 min, obtained via illumination with white light. EDX maps of I and Br in separate x_{Br} =0|1 heterostructures before (c) and after (d) heating at 100°C for 120 min. (e) Interface profiles (halide fraction vs. distance D) of the heterostructures in (a)-(d), showing overlap of the optical microscopy and EDX-determined x_{Br} traces. x_I represents the halide fraction of I obtained from the EDX images (c) and (d) (orange circles). x_{Br} represents the halide fraction of Br obtained from the EDX images (c) and (d) (blue circles) and from the optical microscopy image (a) (blue line). The dashed lines indicate the interface width. The black arrow in (a) and (e) denotes residual PDMS on the heterostructure surface (**Figure S7**), resulting in a dip in optical intensity near ≈ 150 μm.

We verified that optical microscopy provided comparable interfacial profiles to EDX, enabling a measurement of the interface profiles in a quasi-real-time and non-destructive manner (**Figure**

4). The interface profiles of $x_{Br} = 0|1$ obtained before and after heating, using both optical microscopy and EDX, are shown in **Figure 4**. Because the bandgap of MAPbBr$_3$ is ≈ 540 nm and that of MAPbI$_3$ is ≈ 775 nm (**Figure 2b**), when the heterostructures were illuminated with white light, the MAPbI$_3$, the MAPbBr$_3$ and the intermediate mixed-halide regions exhibited very different transmission behavior (**Figure 4a/b**) and thus very different contrast. The dark color in **Figure 4a/b** is MAPbI$_3$, the yellow is MAPbBr$_3$, and the pink is the intermediate region. The images were converted to grayscale by taking the average values of the red, green and blue pixels, giving each pixel equal weight. We then integrated the images to obtain interface profiles, with the darker and lighter areas corresponding to MAPbI$_3$ and MAPbBr$_3$ respectively (**Figure 4e** and **Supporting Information**). Interface profiles obtained from EDX overlapped well with those obtained via optical microscopy (**Figure 4e**), confirming the validity of the optical method. The optical microscopy and EDX interfacial profiles differ at a position of ≈ 150 μm along the interface (black arrows in **Figure 4a/e**), which we attribute to residual PDMS on the sample (**Figure S7**). We assume the EDX trace is more accurate in this region. We subsequently applied the optical method to $x_{Br} = 0.70|1$ and $x_{Br} = 0.12|1$ heterostructures (**Figures 7** and **S10**), again confirming compositions using EDX.
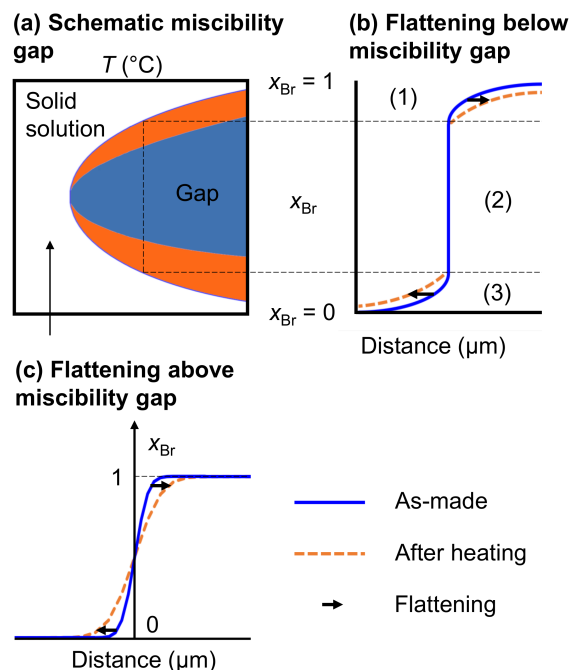
Figure 5. (a) Predicted miscibility gap for the MAPb(Br$_x$I$_{1-x}$)$_3$ system following a regular solution model (from DFT [51]), with expected interface profile behavior (b) when heated to below the gap for a two-phase binary system and (c) when heated to above the gap, for a single-phase binary system. [63] Sections (1) and (3) refer to the Br-rich and I-rich halide miscible regions outside the miscibility gap, and section (2) refers to the halide-immiscible region within the gap. The blue and orange regions designate predicted binodal and spinodal areas of the miscibility gap.

The expected changes in the interface profiles upon exposure to heat strongly depend on whether or not the heterostructure is heated to below or above the miscibility gap. [63,64] **Figure 5** depicts a schematic miscibility gap for the MAPb(Br$_x$I$_{1-x}$)$_3$ system, with approximate interfacial profile shapes before and after heating shown if the heterostructure is kept at temperatures within the miscibility gap (**Figure 5b**) or is heated to above the miscibility gap (**Figure 5c**). For simplicity, the tetragonal-cubic phase transition in the I-rich region is not shown. Within the schematic gap (**Figure 5a** - shaded area), halides are expected to phase separate into I-rich and Br-rich phases. The shape of the interface profile is thus not expected to change for composition regions of the

interfacial profile that are contained within the miscibility gap (**Figure 5b** – section (2)). However, outside of the miscibility gap, halides can still intermix, which should change the shape of the profile away from the interface (**Figure 5b** – sections (1) and (3)). Due to mass balance as halides move from one side to the other, the interface should shift also slightly in location (**Figure 5b**).[63,64] In contrast, should the heterostructures be heated to above the miscibility gap (**Figure 5c**), halides should be free to intermix across the entire interfacial profile. Br and I should thus diffuse down their respective concentration gradients, resulting in apparent flattening of the entire interfacial profile, as shown in **Figure 5c**. This flattening would be most apparent near the edges of the interface (Br-rich and I-rich regions), and least apparent near the mid-point, where the composition stays constant.

Before discussing the response of the interfacial profiles to heat, we first analyzed the behavior of the interfacial profiles upon formation. Although XRD and other characterizations indicated clear presence $x_{Br} = 0$ and $x_{Br} = 1$ in the heterostructure (**Figures 2** and **4**), no XRD peaks corresponding to intermediate compositions were identified (**Figure 2 and S6**), as the interfacial region is a small percentage of the overall area in the incident beam. Given the presence of the gap,[25,51] one might expect the interface to be composed of crystallites with stoichiometries corresponding to the I-rich and Br-rich binodal lines. When averaged, mixtures of different amounts of these crystallites would then yield the apparently-smooth composition profiles of **Figures 4** and **6**. In agreement with this, a MAPbI$_3$ film exposed to Br$_2$ vapor for only 5 seconds (as opposed to 60s required for full bromination) exhibited highly uneven bromination, in the sense that exposure to Br$_2$ vapor induced formation of pockets of Br-rich regions, rather than the even, gradual composition change that would be expected if the compositions were miscible (**Figure S11**). However, emission corresponding to intermediate mixed-halide compositions (605 - 699

nm, or $0.3 < x_{Br} < 0.7$; see discussion of **Figure S5**) was observed in the interfacial region via scanning confocal microscopy (**Figures 2b** and **S5**), where sample exposure times are on the order of microseconds, indicating some retention of the $0.3 < x_{Br} < 0.7$ compositions. Prolonged exposure to above-bandgap light (405 nm, or 3.06 eV) induced a red-shifting photoluminescence emission at 730 nm (1.7 eV) that also became more intense over time, which is characteristic of light-induced phase separation into I-rich and Br-rich regions[20] (**Figure S12**), and suggests that some intermediate compositions were present initially. Given all these observations, it is likely that upon formation, the interface was composed of some metastable intermediate compositions, as well as of some phase separated nanoscale I-rich and Br-rich regions (**Figures 2b** and **S5**).
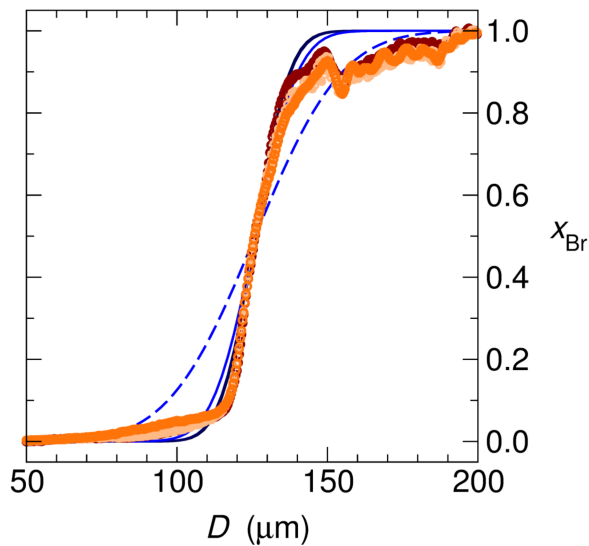

Figure 6. Compositional profiles of an $x_{Br} = 0|1$ heterostructure obtained using optical microscopy after 0 min, 120 min, 260 min and 360 min of heating at 100°C. Profiles from Fick's second law with different interdiffusion coefficients D_i were calculated as described in **Section S9**.
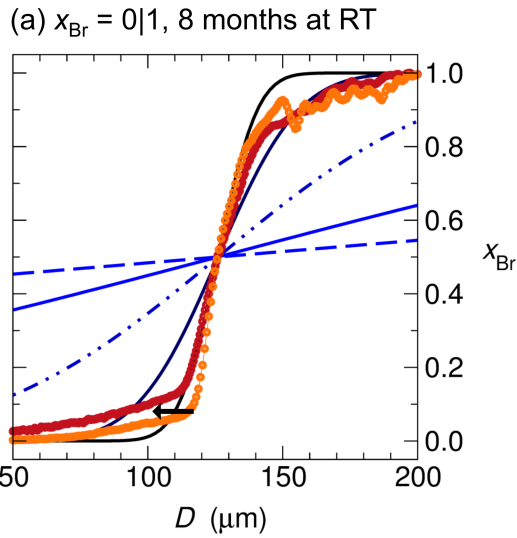
We then examined the effects of heating on the interfacial profiles. All heterostructures studied exhibited little interfacial profile flattening upon heat exposure (**Figures 6, 7, S10** and **S15**). Slight changes in composition near $x_{Br} = 0.8$ and $x_{Br} = 0.1$ were observed in $x_{Br} = 0|1$ after heating at 100°C for 360 min (**Figure 6**); however, overall, the interfacial profiles changed very little. The profiles do not follow Fickian behavior described by **Figure 5c**, i.e. what would be expected from a solid solution (see **Figure S13**). Calculations of how the diffusion profile should change according to Fick's law (see **Section S9** of the **Supporting Information**) with interdiffusion coefficients D_i of different magnitudes were overlaid with the interfacial profiles for comparison (Figure **6**). Although there is some uncertainty of the profile derived from microscopy at higher values of x_{Br}, D_i cannot be larger than $\sim 10^{-11}$ cm^2/s at 100° C based on examination of the profile on both sides of the interface. The profiles of the $x_{Br} = 0.12|1$ and $x_{Br} = 0.70|1$ heterostructures were also unchanged upon heating at 100°C for 260 min by microscopy and EDX (**Figures 7** and **S10, S14**). We thus take $D_i \leq 10^{-11}$ cm^2/s as an upper bound of the interdiffusion coefficient for MAPb(Br$_x$I$_{1-x}$)$_3$ at 100°C. Such a value is consistent with D_i obtained at lower temperatures and in different systems, namely 3×10^{-12} cm^2/s at 50°C using PbBr$_2$ as a Br-source for a PbBr$_2$-MAPbI$_3$ heterostructure[29] and $\sim 1 \times 10^{-12}$ cm^2/s at room temperature for a CsPbBr$_3$-MAPbI$_3$ heterostructure.[49] However, the poor fit to this model suggests an alternative explanation.
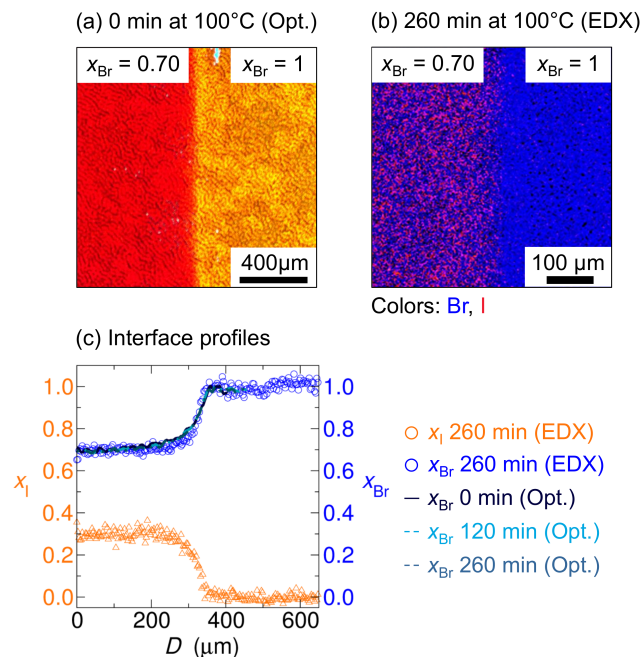
Figure 7. (a) Optical microscopy image of an $x_{Br} = 0.70|1$ heterostructure before heating. (b) EDX mapping of I and Br in the same $x_{Br} = 0.70|1$ heterostructure (in the same location) after heating at 100°C for 260 min. (c) Interface profiles (halide fraction vs. distance D) of the same $x_{Br} = 0.70|1$ heterostructure upon heating to 100°C for varying amounts of time. x_I represents the halide fraction of I obtained from the EDX image (b) (orange circles). x_{Br} represents the halide fraction of Br obtained from the EDX image (b) (blue circles) as well as from the optical microscopy image (a) (black line). Additional interface profiles obtained via optical microscopy are included (dashed blue lines).

The lack of flattening of the interfacial region may indicate slow interdiffusion, but if the miscibility gap extends to higher temperatures than predicted then we would expect different behavior than that of **Figure 5c**. The changes in the interface profile at 100°C were slight and only at the edges of the interface profiles (**Figure 6**), much like the interfacial profiles depicted in **Figure 5b**. No large changes were observed in $x_{Br} = 0.12|1$ and in $x_{Br} = 0.70|1$ heterostructures upon heating at 100°C for 260 min (**Figures 7** and **S10**). The interfacial profiles were all set to overlap at $x_{Br} = 0.5$ during analysis and we do not have a marker to track changes in the interfacial profile shifted in location as in **Figure 5b**. We also examined a $x_{Br} = 0|1$ formed using another

route to for the initial MAPbI$_3$ layer and found similar behavior (**Figure S15**). Overall, these results

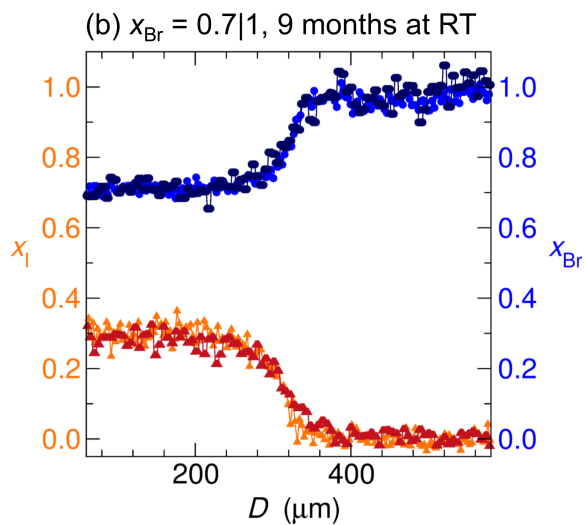suggest a miscibility gap extending to above 100°C and well into the Br-rich region.

(a) $x_{Br} = 0|1$, 8 months at RT

Time at RT:

○ 0 months
○ 8 months

— Sim. 0 min
← Flattening

Sim. D_i, 8 months:

—— 10^{-13} cm²/s
—·— 10^{-12} cm²/s
—— 10^{-11} cm²/s
— — 10^{-10} cm²/s

(b) $x_{Br} = 0.7|1$, 9 months at RT

**Time at RT:**
▸—▸ x_I 0 months
▴—▴ x_I 9 months
•—• x_{Br} 0 months
•—• x_{Br} 9 months

Figure 8. Effects of 8-9 months of storage at room temperature on the interfacial profiles of (a) $x_{Br} = 0|1$ and (b) $x_{Br} = 0.70|1$, with overlapping simulations of Fick's law with different D_i and interfacial profile flattening (black arrow).

To rule out the possibility of slow interdiffusion at room temperature, we then examined the response of interfacial profiles to long-term storage (8-9 months), to determine the composition bounds of the miscibility gap at room temperature. All encapsulated heterostructures (x_{Br} =0|1, x_{Br} =0.12|1 and x_{Br} =0.70|1) were stored at room temperature in ambient for 8 to 9 months, after which the interfacial profiles were again obtained via a combination of optical microscopy and EDX (**Figures 8**, **S10** and **S16**). We show the profiles expected for simple diffusion in the absence of a miscibility gap for a range of interdiffusion constants. Even for values as low as ~10^{-13} cm^2/s at this timescale we would expect a substantial change in the profile on both sides of the midpoint which is not observed. A noticeable change towards higher concentration of iodide was observed in the composition region from $0 < x_{Br} < 0.2$ in x_{Br} =0|1 stored for 8 months, consistent with the presence of a solid solution region from $0 < x_{Br} < 0.2$ (**Figure 8a**).[20,51,65] Based on the distance that the composition shifted (≈ 20 μm), D_i in this region would be $\approx 10^{-13}$ cm^2/s, which is lower than the D_i estimated in the I-rich region of a CsPbBr$_3$-MAPbI$_3$ heterostructure at room temperature.[49] In contrast, little change was observed in the composition region $0.2 < x_{Br} < 1.0$ in x_{Br} =0|1 (**Figure 8a**), consistent with the presence of a miscibility gap for $0.2 < x_{Br} < 1.0$. The behavior of the profile, particularly the region near $x_{Br} \approx 0.2$, is consistent with the presence of a miscibility gap (**Figure 5b**), in general agreement with the predicted phase diagram by DFT. To further probe the extent of the gap into the Br-rich region, we compared the interfacial profiles of x_{Br} =0.70|1 before and after 9 months of storage, via EDX. No flattening was observed, suggesting that the miscibility gap extends to very near $x_{Br} = 1$ at room temperature (**Figure 9**), which is much further into the Br-rich region than predicted by theory.[51] Extension of the gap to $x_{Br} \approx 1$ may explain why mixed Br-I hybrid of very high Br-content (e.g. $x_{Br} = 0.9$) have been observed to undergo light-induced phase separation.[20] Because we cannot access longer times for interdiffusion at elevated

temperatures, we cannot completely rule out that diffusion is simply slow which limits our ability to set the temperature for the miscibility gap. Such very slow interdiffusion would be consistent with the slower re-mixing of halides in the dark, after light-induced phase separation, the latter of which is typically a rapid process. [20,21] **Figure 9** shows three possibilities constrained by the magnitude of the interdiffusion constant.
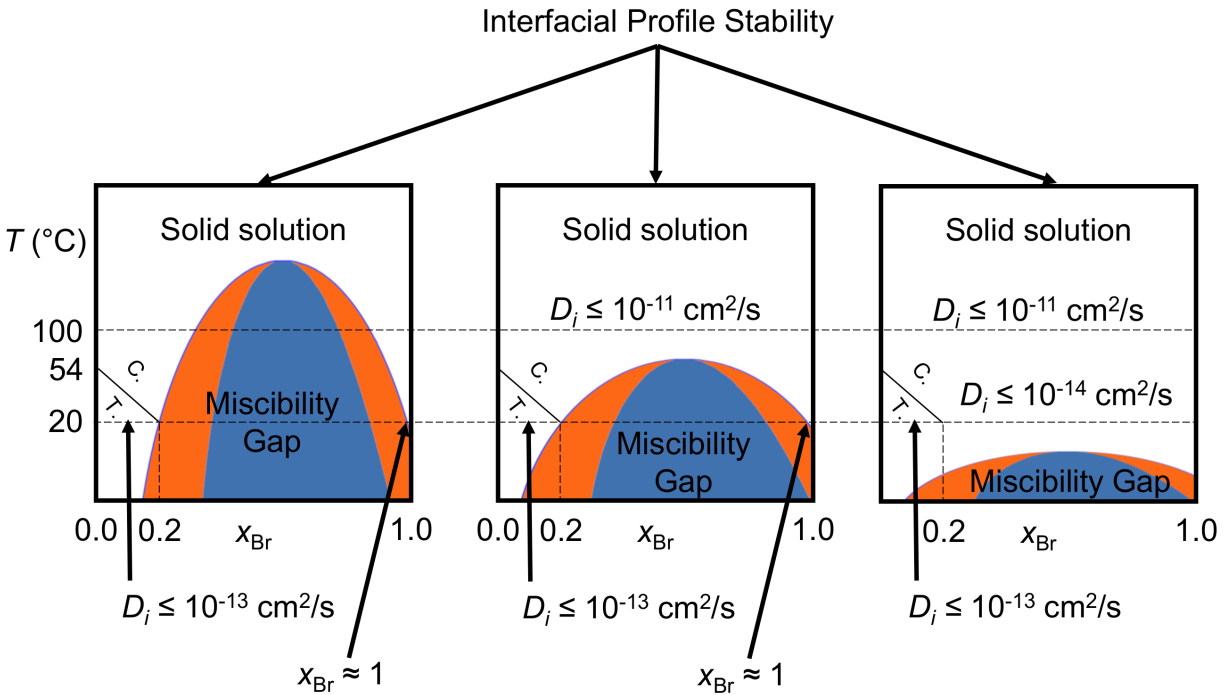
Figure 9. Summary of results, with three possible explanations for the obtained data, and with the Br-rich binodal line at room temperature near $x_{Br} = 1$. Schematic phase diagrams for the $MAPb(Br_xI_{1-x})_3$ system, modified from reference,[51] should the miscibility gap either extend to above 100°C or extend to below 100°C, with the obtained upper bounds for D_i at room temperature and 100°C. C. and T. refer to cubic (*Pm-3m*) [26] and tetragonal (*I4/mcm*)[58] phases respectively, with phase transition temperatures for the $x_{Br} = 0.0$ and $x_{Br} = 0.2$ compositions reported from references.[33,66] The blue and orange regions designate binodal and spinodal areas of the miscibility gap, respectively.

Finally, we examined the response of an $x_{Br} = 0|1$ heterostructure to light (**Figure 10**). Light-induced spinodal decomposition has been observed in single-crystal nanowires of $MAPb(Br_xI_{1−x})_3$, where halides diffused up the concentration gradient.[25] We would thus not expect interface profile flattening when exposing an $x_{Br} = 0|1$ heterostructure to light, but rather the formation of I-rich and Br-rich regions along the interface. Consistent with these expectations, prolonged exposure of the interface region to above-bandgap light (3.06 eV) at ≈ 0.14 Suns (≈ 14 mW/cm²) induced the growing and red-shifting photoluminescence emission at 1.7 eV characteristic of light-induced phase separation into I-rich and Br-rich regions (**Figure S12**).[20] Previous works also reported that the I-rich domains formed during spinodal decomposition are sub-100 nm[20,23] in polycrystalline $MAPb(Br_xI_{1-x})_3$, which is below the resolution of our experiment. We tested the response of the interfacial profiles of an $x_{Br} = 0|1$ heterostructure to light by exposing the whole heterostructure to 1 Sun (AM 1.5G, 100 mW/cm²) of light for 360 min (**Figure 10**) at room temperature. In agreement with expectations, the interfacial profile of $x_{Br} = 0|1$ did not change after light exposure, providing additional confirmation that light does not activate long-range halide transport in mixed-halide perovskite thin films.
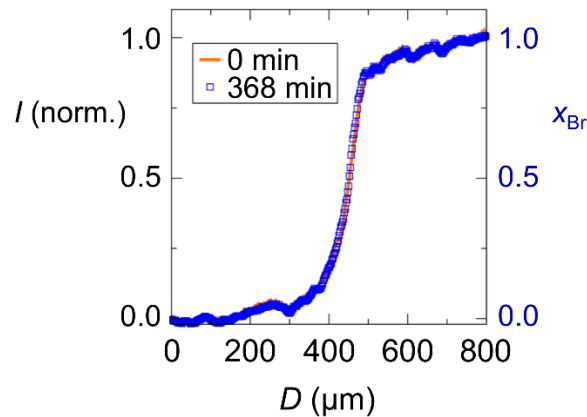
Figure 10. Integrated interfacial profiles of an $x_{Br} = 0|1$ heterostructure before and after exposure to 1 Sun for 368 min, with corresponding x_{Br} axis shown on the right.

CONCLUSIONS

In conclusion, we have examined interdiffusion in planar heterostructures of MAPb(Br$_x$I$_{1-x}$)$_3$ films. These structures did not undergo simple interdiffusion that would be expected for a miscible system, but were more consistent with the presence of a miscibility gap at 100 °C. We also determined the upper bound of the bromide-iodide interdiffusion coefficient ($D_i \leq 10^{-11}$ cm^2/s) in spin-coated MAPb(Br$_x$I$_{1-x}$)$_3$ films at 100°C. Long term study of the interface indicates that the binodal line at room temperature extends to higher fractional composition of bromine than predicted by theory, but is in reasonable agreement at high iodide composition. Improvement of our understanding of the phase diagram of MAPb(Br$_x$I$_{1-x}$)$_3$ will help to explain the origin of light-induced phase separation observed in very Br-rich mixed halide perovskites.

ASSOCIATED CONTENT

Supporting Information. Experimental section including heterostructure fabrication, as well as various characterizations including SEM, EDX, confocal microscopy, XRD, UV-Vis, and interface profile response to light exposure, interface profile fitting and *J-V* curve certifying that the MAPbI$_3$ used yields solar cells of high efficiency. (PDF)

AUTHOR INFORMATION

ORCID.
Rhys M. Kennard: 0000-0003-1181-5638
Michael L. Chabinyc: 0000-0003-4641-3508

Notes

The authors declare no competing financial interest.

REFERENCES

(1)   Yang, W. S.; Park, B.-W.; Jung, E. H.; Jeon, N. J. Iodide Management in Formamidinium-Lead-Halide - Based Perovskite Layers for Efficient Solar Cells. *Science (80).* **2017**, *356* (6345), 1376 - 1379.

(2)   Blakers, A.; Zin, N.; McIntosh, K. R.; Fong, K. High Efficiency Silicon Solar Cells. *Energy Procedia* **2013**, *33*, 1 - 10.

(3)   Kojima, A.; Teshima, K.; Shirai, Y.; Miyasaka, T. Organometal Halide Perovskites as Visible - Light Sensitizers for Photovoltaic Cells. *J Am Chem Soc* **2009**, *131* (October), 6050 - 6051.

(4)   Stoumpos, C. C.; Malliakas, C. D.; Kanatzidis, M. G. Semiconducting Tin and Lead Iodide Perovskites with Organic Cations: Phase Transitions, High Mobilities, and near-Infrared Photoluminescent Properties. *Inorg. Chem.* **2013**, *52* (15), 9019 - 9038.

(5)   Lee, M. M.; Teuscher, J.; Miyasaka, T.; Murakami, T. N.; Snaith, H. J. Efficient Hybrid Solar Cells Based on Meso-Superstructured Organometal Halide Perovskites. *Science (80).* **2012**, *338* (November), 1209 - 1214.

(6)   Berry, J.; Buonassisi, T.; Egger, D. A.; Hodes, G.; Kronik, L.; Loo, Y. L.; Lubomirsky, I.; Marder, S. R.; Mastai, Y.; Miller, J. S.; Mitzi, D. B.; Paz, Y.; Rappe, A. M.; Riess, I.; Rybtchinski, B.; Stafsudd, O.; Stevanovic, V.; Toney, M. F.; Zitoun, D.; Kahn, A.; Ginley, D.; Cahen, D.Hybrid Organic-Inorganic Perovskites (HOIPs): Opportunities and Challenges. *Adv. Mater.* **2015**, *27* (35), 5102 - 5112.

(7)   Zhao, D.; Wang, C.; Song, Z.; Yu, Y.; Chen, C.; Zhao, X.; Zhu, K.; Yan, Y. Four-Terminal All-Perovskite Tandem Solar Cells Achieving Power Conversion Efficiencies Exceeding 23%. *ACS Energy Lett.* **2018**, *3* (2), 305 - 306.

(8)   Saliba, M.; Matsui, T.; Seo, J. Y.; Domanski, K.; Correa-Baena, J. P.; Nazeeruddin, M. K.; Zakeeruddin, S. M.; Tress, W.; Abate, A.; Hagfeldt, A.; Grätzel, M. Cesium-Containing Triple Cation Perovskite Solar Cells: Improved Stability, Reproducibility and High Efficiency. *Energy Environ. Sci.* **2016**, *9* (6), 1989 - 1997.

(9)   Yi, C.; Luo, J.; Meloni, S.; Boziki, A.; Ashari-Astani, N.; Grätzel, C.; Zakeeruddin, S. M.; Röthlisberger, U.; Grätzel, M. Entropic Stabilization of Mixed A-Cation ABX_3 Metal Halide Perovskites for High Performance Perovskite Solar Cells. *Energy Environ. Sci.* **2016**,

9 (2), 656 - 662.

(10)   McMeekin, D. P.; Sadoughi, G.; Rehman, W.; Eperon, G. E.; Saliba, M.; Horantner, M. T.; Haghighirad, A.; Sakai, N.; Korte, L.; Rech, B.; Johnston, M. B.; Herz, L. M.; Snaith, H. J. A Mixed-Cation Lead Mixed-Halide Perovskite Absorber for Tandem Solar Cells. *Science (80).* **2016**, *351* (6269), 151 - 155.

(11)   Jeon, N. J.; Noh, J. H.; Yang, W. S.; Kim, Y. C.; Ryu, S.; Seo, J.; Seok, S. Il. Compositional Engineering of Perovskite Materials for High-Performance Solar Cells. *Nature* **2015**, *517* (7535), 476 - 480.

(12)   Ono, L. K.; Juarez-Perez, E. J.; Qi, Y. Progress on perovskite materials and solar cells with mixed cations and halide anions. *ACS Appl. Mater. Interfaces* **2017**, *9* (36), 30197-30246.

(13)   Zhang, Y.; Grancini, G.; Feng, Y.; Asiri, A. M.; Nazeeruddin, M. K. Optimization of Stable Quasi-Cubic $FA_xMA_{1-x}PbI_3$ Perovskite Structure for Solar Cells with Efficiency beyond 20%. *ACS Energy Lett.*, **2017**, *2*(4), 802-806.

(14)   Dai, J.;, Fu, Y.; Manger, L. H.; Rea, M. T.; Hwang, L.; Goldsmith, R. H.; Jin, S. Carrier Decay Properties of Mixed Cation Formamidinium–Methylammonium Lead Iodide Perovskite $[HC(NH_2)_2]_{1-x}[CH_3NH_3]_xPbI_3$ Nanorods. *J. Phys. Chem. Lett.*, **2016**, *7* (24), 5036-5043.

(15)   Protesescu, L.; Yakunin, S.; Bodnarchuk, M. I.; Krieg, F.; Caputo, R.; Hendon, C. H.; Yang, R. X.; Walsh, A.; Kovalenko, M. V. Nanocrystals of Cesium Lead Halide Perovskites $(CsPbX_3, X = Cl, Br, and I)$: Novel Optoelectronic Materials Showing Bright Emission with Wide Color Gamut. *Nano Lett.* **2015**, *15* (6), 3692–3696.

(16)   Song, J.; Li, J.; Li, X.; Xu, L.; Dong, Y.; Zeng, H. Quantum Dot Light-Emitting Diodes Based on Inorganic Perovskite Cesium Lead Halides $(CsPbX_3)$. *Adv. Mater.* **2015**, *27* (44), 7162 - 7167.

(17)   Walsh, A.; Stranks, S. D. Taking control of ion transport in halide perovskite solar cells. *ACS Energy Lett.*, **2018**, *3* (8), 1983-1990.

(18)   Azpiroz, J. M.; Mosconi, E.; Bisquert, J.; De Angelis, F. Defect Migration in Methylammonium Lead Iodide and Its Role in Perovskite Solar Cell Operation. *Energy Environ. Sci.* **2015**, *8* (7), 2118 - 2127.

(19)   Snaith, H. J.; Abate, A.; Ball, J. M.; Eperon, G. E.; Leijtens, T.; Noel, N. K.; Stranks, S. D.; Wang, J. T. W.; Wojciechowski, K.; Zhang, W. Anomalous Hysteresis in Perovskite Solar

Cells. *J. Phys. Chem. Lett.* **2014**, *5* (9), 1511 - 1515.

(20)   Hoke, E. T.; Slotcavage, D. J.; Dohner, E. R.; Bowring, A. R.; Karunadasa, H. I.; Mcgehee, M. D. Reversible Photo-Induced Trap Formation in Mixed- Halide Hybrid Perovskites for Photovoltaics. *Chem. Sci.* **2015**, *6*, 613-317.

21)   Draguta, S.; Sharia, O.; Yoon, S. J.; Brennan, M. C.; Morozov, Y. V.; Manser, J. M.; Kamat, P. V.; Schneider, W. F.; Kuno, M. Rationalizing the Light-Induced Phase Separation of Mixed Halide Organic-Inorganic Perovskites. *Nat. Commun.* **2017**, *8* (1).

(22)   Barker, A. J.; Sadhanala, A.; Deschler, F.; Gandini, M.; Senanayak, S. P.; Pearce, P. M.; Mosconi, E.; Pearson, A. J.; Wu, Y.; Ram Srimath Kandada, A.; Leijtens, T; De Angelis, F.; Dutton, S. E.; Petrozza, A.; Friend, R. H. Defect-Assisted Photoinduced Halide Segregation in Mixed-Halide Perovskite Thin Films. *ACS Energy Lett.* **2017**, *2*, 1416–1424.

(23)   Bischak, C. G.; Hetherington, C. L.; Wu, H.; Aloni, S.; Ogletree, D. F.; Limmer, D. T.; Ginsberg, N. S. Origin of Reversible Photo-Induced Phase Separation in Hybrid Perovskites. *Nano Lett.* **2017**, *17*, 1028 - 1033.

(24)   Yoon, S. J.; Kuno, M.; Kamat, P. V. Shift Happens. How Halide Ion Defects Influence Photoinduced Segregation in Mixed Halide Perovskites. *ACS Energy Lett.* **2017**, *2*, 1507 - 1514.

(25)   Wang, Y.; Chen, Z.; Deschler, F.; Sun, X.; Lu, T. M.; Wertz, E. A.; Hu, J. M.; Shi, J. Epitaxial Halide Perovskite Lateral Double Heterostructure. *ACS Nano* **2017**, *11* (3), 3355 - 3364.

(26)   Jaffe, A.; Lin, Y.; Beavers, C. M.; Voss, J.; Mao, W. L.; Karunadasa, H. I. High-Pressure Single-Crystal Structures of 3D Lead-Halide Hybrid Perovskites and Pressure Effects on Their Electronic and Optical Properties. *ACS Cent. Sci.* **2016**, *2*, 201 - 209.

(27)   Marongiu, D.; Chang, X.; Sarritzu, V.; Sestu, N.; Pau, R.; Geddo Lehmann, A.; Mattoni, A.; Quochi, F.; Saba, M.; Mura, A.; Bongiovanni, G. Self-Assembled Lead Halide Perovskite Nanocrystals in a Perovskite Matrix. *ACS Energy Lett.* **2017**, *2* (4), 769 - 775.

(28)   Yang, X.; Yan, X.; Wang, W.; Zhu, X.; Li, H.; Ma, W.; Sheng, C. X. Light Induced Metastable Modification of Optical Properties in $CH_3NH_3PbI_{3-x}Br_x$ Perovskite Films: Two-Step Mechanism. *Org. Electron. physics, Mater. Appl.* **2016**, *34*, 79 - 83.

(29)   Xing, J.; Wang, Q.; Dong, Q.; Yuan, Y.; Fang, Y.; Huang, J. Ultrafast Ion Migration in Hybrid Perovskite Polycrystalline Thin Films under Light and Suppression in Single

Crystals. *Phys. Chem. Chem. Phys.* **2016**, *18* (44), 30484 - 30490.

(30) Yoon, S. J.; Draguta, S.; Manser, J. S.; Sharia, O.; Schneider, W. F.; Kuno, M.; Kamat, P. V. Tracking Iodide and Bromide Ion Segregation in Mixed Halide Lead Perovskites during Photoirradiation. *ACS Energy Lett.* **2016**, *1* (1), 290 - 296.

(31) Slotcavage, D. J.; Karunadasa, H. I.; McGehee, M. D. Light-Induced Phase Segregation in Halide-Perovskite Absorbers. *ACS Energy Lett.* **2016**, *1* (6), 1199 - 1205.

(32) Samu, G. F.; Janáky, C.; Kamat, P. V. A Victim of Halide Ion Segregation. How Light Soaking Affects Solar Cell Performance of Mixed Halide Lead Perovskites. *ACS Energy Lett.* **2017**, *2* (8), 1860 - 1861.

(33) Noh, J. H.; Im, S. H.; Heo, J. H.; Mandal, T. N.; Seok, S. Il. Chemical Management for Colorful, Efficient, and Stable Inorganic - Organic Hybrid Nanostructured Solar Cells. *Nano Lett.* **2013**, *13*, 1764 - 1769.

(34) Suarez, B.; Gonzalez-Pedro, V.; Ripolles, T. S.; Sanchez, R. S.; Otero, L.; Mora-Sero, I. Recombination Study of Combined Halides (Cl, Br, I) Perovskite Solar Cells. *J. Phys. Chem. Lett.* **2014**, *5* (10), 1628 - 1635.

(35) Kulkarni, S. A.; Baikie, T.; Boix, P. P.; Yantara, N.; Mathews, N.; Mhaisalkar, S. Band-Gap Tuning of Lead Halide Perovskites Using a Sequential Deposition Process. *J. Mater. Chem. A* **2014**, *2* (24), 9221 - 9225.

(36) Eperon, G. E.; Stranks, S. D.; Menelaou, C.; Johnston, M. B.; Herz, L. M.; Snaith, H. J. Formamidinium Lead Trihalide: A Broadly Tunable Perovskite for Efficient Planar Heterojunction Solar Cells. *Energy Environ. Sci.* **2014**, *7* (3), 982 - 988.

(37) Balakrishna, R. G.; Kobosko, S. M.; Kamat, P. V. Mixed Halide Perovskite Solar Cells. Consequence of Iodide Treatment on Phase Segregation Recovery. *ACS Energy Lett.* **2018**, (3), 2267 - 2272.

(38) Meloni, S.; Moehl, T.; Tress, W.; Franckevičius, M.; Saliba, M.; Lee, Y. H.; Gao, P.; Nazeeruddin, M. K.; Zakeeruddin, S. M.; Rothlisberger, U.; Graetzel, M. Ionic Polarization-Induced Current - Voltage Hysteresis in $CH_3NH_3PbX_3$ Perovskite Solar Cells. *Nat. Commun.* **2016**, *7* (May 2015), 10334.

(39) Zhang, T.; Chen, H.; Bai, Y.; Xiao, S.; Zhu, L.; Hu, C.; Xue, Q.; Yang, S. Understanding the Relationship between Ion Migration and the Anomalous Hysteresis in High-Efficiency Perovskite Solar Cells: A Fresh Perspective from Halide Substitution. *Nano Energy* **2016**,

26, 620 - 630.

(40) Eames, C.; Frost, J. M.; Barnes, P. R. F.; O'Regan, B. C.; Walsh, A.; Islam, M. S. Ionic Transport in Hybrid Lead Iodide Perovskite Solar Cells. *Nat. Commun.* **2015**, *6* (May), 7497.

(41) Hoque, M. N. F.; Islam, N.; Zhu, K.; Fan, Z. Hybrid Perovskite Phase Transition and Its Ionic, Electrical and Optical Properties. *MRS Adv.* **2017**, *2* (53), 3077-3082.

(42) Haruyama, J.; Sodeyama, K.; Han, L.; Tateyama, Y. First-Principles Study of Ion Diffusion in Perovskite Solar Cell Sensitizers. *J. Am. Chem. Soc.* **2015**, *137* (32), 10048 - 10051.

(43) Li, D.; Wu, H.; Cheng, H. C.; Wang, G.; Huang, Y.; Duan, X. Electronic and Ionic Transport Dynamics in Organolead Halide Perovskites. *ACS Nano* **2016**, *10* (7), 6933 - 6941.

(44) Ming, W.; Chen, S.; Du, M. H. Chemical Instability Leads to Unusual Chemical-Potential-Independent Defect Formation and Diffusion in Perovskite Solar Cell Material $CH_3NH_3PbI_3$. *J. Mater. Chem. A* **2016**, *4* (43), 16975 - 16981.

(45) Zhao, Y.-C.; Zhou, W.-K.; Zhou, X.; Liu, K.-H.; Yu, D.-P.; Zhao, Q. Quantification of Light-Enhanced Ionic Transport in Lead Iodide Perovskite Thin Films and Its Solar Cell Applications. *Light Sci. Appl.* **2016**, *6* (5), 16243.

(46) Głowienka, D.; Miruszewski, T.; Szmytkowski, J. The Domination of Ionic Conductivity in Tetragonal Phase of the Organometal Halide Perovskite $CH_3NH_3PbI_{3-x}Cl_x$. *Solid State Sci.* **2018**, *82* (May), 19 - 23.

(47) Game, O. S.; Buchsbaum, G. J.; Zhou, Y.; Padture, N. P.; Kingon, A. I. Ions Matter: Description of the Anomalous Electronic Behavior in Methylammonium Lead Halide Perovskite Devices. *Adv. Funct. Mater.* **2017**, *27* (16), 1606584.

(48) Delugas, P.; Caddeo, C.; Filippetti, A.; Mattoni, A. Thermally Activated Point Defect Diffusion in Methylammonium Lead Trihalide: Anisotropic and Ultrahigh Mobility of Iodine. *J. Phys. Chem. Lett.* **2016**, *7* (13), 2356 - 2361.

(49) Pan, D.; Fu, Y.; Chen, J.; Czech, K. J.; Wright, J. C.; Jin, S. Visualization and Studies of Ion-Diffusion Kinetics in Cesium Lead Bromide Perovskite Nanowires. *Nano Lett.* **2018**, *18* (3), 1807 - 1813.

(50) Lai, M.; Obliger, A.; Lu, D.; Kley, C. S.; Bischak, C. G.; Kong, Q.; Lei, T. Intrinsic Anion Diffusivity in Lead Halide Perovskites Is Facilitated by a Soft Lattice. **2018**, *115* (47), 2 - 7.

(51) Brivio, F.; Caetano, C.; Walsh, A. Thermodynamic Origin of Photoinstability in the $CH_3NH_3Pb(I_{1-x}Br_x)_3$ Hybrid Halide Perovskite Alloy. *J. Phys. Chem. Lett.* **2016**, *7*, 1083 - 1087.

(52) Bechtel, J. S.; Van Der Ven, A. First-Principles Thermodynamics Study of Phase Stability in Inorganic Halide Perovskite Solid Solutions. *Phys. Rev. Mater. 2* **2018**, *045401*, 1 - 7.

(53) Solis-Ibarra, D.; Smith, I. C.; Karunadasa, H. I. Post-Synthetic Halide Conversion and Selective Halogen Capture in Hybrid Perovskites. *Chem. Sci.* **2015**, *6* (7), 4054 - 4059.

(54) Shewmon, N. T.; Yu, H.; Constantinou, I.; Klump, E.; So, F. Formation of Perovskite Heterostructures by Ion Exchange. *ACS Appl. Mater. Interfaces* **2016**, *8* (48), 33273 - 33279.

(55) Dou, L.; Lai, M.; Kley, C. S.; Yang, Y.; Bischak, C. G.; Zhang, D.; Eaton, S. W.; Ginsberg, N. S.; Yang, P. Spatially Resolved Multicolor $CsPbX_3$ Nanowire Heterojunctions via Anion Exchange. *Proc. Natl. Acad. Sci.* **2017**, 201703860.

(56) Tian, W.; Leng, J.; Zhao, C.; Jin, S. Long-Distance Charge Carrier Funneling in Perovskite Nanowires Enabled by Built-in Halide Gradient. *J. Am. Chem. Soc.* **2017**, *139* (2), 579 - 582.

(57) Rothmann, M. U.; Li, W.; Zhu, Y.; Liu, A.; Ku, Z.; Bach, U.; Etheridge, J.; Cheng, Y. Structural and Chemical Changes to $CH_3NH_3PbI_3$ Induced by Electron and Gallium Ion Beams. *Adv. Mater.* **2018**, *30* (25), 1800629.

(58) Yamada, Y.; Yamada, T.; Phuong, L. Q.; Maruyama, N.; Nishimura, H.; Wakamiya, A.; Murata, Y.; Kanemitsu, Y. Dynamic Optical Properties of $CH_3NH_3PbI_3$ Single Crystals As Revealed by One - and Two - Photon Excited Photoluminescence Measurements. *J. Am. Chem. Soc.* **2015**, *137* (33), 10456 - 10459.

(59) Khanna, S.; Sundaram, S.; Reddy, K. S.; Mallick, T. K. Performance Analysis of Perovskite and Dye-Sensitized Solar Cells under Varying Operating Conditions and Comparison with Monocrystalline Silicon Cell. *Appl. Therm. Eng.* **2017**, *127*, 559 - 565.

(60) Xue, H.; Ruan, W.; Zhang, M.; Rong, M. Fast Curing Ethylene Vinyl Acetate Films with Dual Curing Agent towards Application as Encapsulation Materials for Photovoltaic Modules. **2014**, *8* (2), 116 - 122.

(61) Drabczyk, K.; Panek, P. A Comparative Study of EVA with and without Thermal History for Different Lamination Process Parameters. *Mater. Sci. Eng. B* **2012**, *177* (15), 1378 -

1383.

(62) Baranwal, A. K.; Kanaya, S.; Peiris, T. A. N.; Mizuta, G.; Nishina, T.; Kanda, H.; Miyasaka, T.; Segawa, H.; Ito, S. 100°C Thermal Stability of Printable Perovskite Solar Cells Using Porous Carbon Counter Electrodes. *ChemSusChem* **2016**, *9* (18), 2604 - 2608.

(63) Shewmon, P. G. *Diffusion in Solids.*; Springer, 2016; Vol. 36.

(64) Balluffi, R. W.; Allen, S. J.; Carter, C. W. *Kinetics of Materials*; John Wiley & Sons: Hoboken, NJ, 2005.

(65) Nandi, P.; Giri, C.; Swain, D.; Manju, U.; Mahanti, S. D. B.; Topwal, D. Temperature Dependent Photo-Induced Reversible Phase Separation in Mixed Halide Perovskite. *ACS Appl. Energy Mater.* **2018**, *1*, 3807 - 3814.

(66) Onada-Yamamur, N.; Matsuo, T.; Suga, H. Calorimetric and IR Spectroscopic Studies of Phase Transitions in Methylammonium Trihalogenoplumbates (II). *J. Phys. Chem. Solids* **1990**, *51* (12), 1383 - 1395.

TOC GRAPHICS
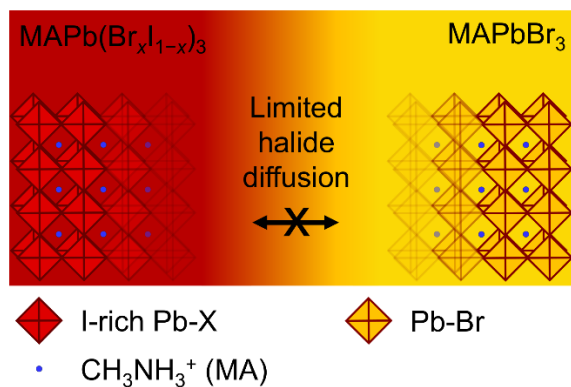
Supporting Information

Phase Stability and Diffusion in Lateral Heterostructures of Methyl Ammonium Lead Halide Perovskites

Rhys M. Kennard, † Clayton J. Dahlman, † Hidenori Nakayama, †§ Ryan A. DeCrescent, § Jon A. Schuller, ‖ Ram Seshadri, †‡ Kunal Mukherjee † and Michael L. Chabinyc †*

† Materials Department, University of California, Santa Barbara, California 93106, United States

§Electronics Materials and New Energy Laboratory, Mitsubishi Chemical Corporation, Yokohama R&D Center 1000, Kamoshida-cho, Aoba-ku, Yokohama 227-8502, Japan

§ Department of Physics, University of California, Santa Barbara, California 93106, United States

‖ Department of Electrical and Computer Engineering, University of California, Santa Barbara, California 93106, United States

‡ Department of Chemistry & Biochemistry, University of California Santa Barbara, Santa Barbara, CA 93106-9510

Corresponding Author

*Email: mchabinyc@engineering.ucsb.edu

Contents

Methods

Materials

Lead (II) iodide was purchased from Sigma Aldrich (PbI$_2$ – 99.999% purity, trace metal basis) and from TCI chemicals (PbI$_2$ – 99.99% purity, trace metal basis). Methylammonium iodide (CH$_3$NH$_3$I, ≥ 99% purity) was purchased from Dyseol. Lead (II) bromide (PbBr$_2$ – 99.999% purity, trace metal basis) and methylammonium bromide (CH$_3$NH$_3$Br – 98% purity) were purchased from Sigma Aldrich. PolyDiMethylSiloxane (PDMS) was fabricated from a Sylgard 184 elastomer kit. N-N-dimethylformamide (DMF, 99.8%, anhydrous), dimethyl sulfoxide (DMSO, ≥ 99.9%, anhydrous), Chlorobenzene (99.8%, anhydrous) were purchased from Sigma Aldrich and kept in a nitrogen glove box. γ-butyl lactone (GLB, ≥ 99%) was purchase from Sigma Aldrich and stored in air. Bromine (Br$_2$, 99.5% purity) liquid was purchased from Alpha Aesar and stored in air. Quartz substrates (z-cut, seedless, 15 × 15 × 0.5 mm) were purchased from University Wafer. Polytriarylamine (PTAA), polyethylenimine (PEIE, 37% aqueous solution) were purchased from Sigma Aldrich and phenyl-C61-butyric acid methyl ester (PCBM, ≥ 99%) was purchased from Nano C.

Spin-casting of I-rich perovskites for heterostructures

Quartz substrates were ultrasonicated for 10 min in acetone and then for 10 min in isopropyl alcohol. The substrates were then exposed to oxygen plasma at ~300 mTorr for 10 min, with air as the oxygen source. Precursor solutions were fabricated in a nitrogen-filled glove box. PbI$_2$ and CH$_3$NH$_3$I were dissolved in 1 mL DMF and 96 μL DMSO to make a 1M solution, and the mixture was stirred for at least 30 min in a nitrogen-filled glove box. The same procedure was applied to precursors PbBr$_2$ and CH$_3$NH$_3$Br. The two solutions were then mixed in stoichiometric ratios necessary to obtain the desired perovskites (e.g. 3 parts I-solution and 7 parts Br-solution to obtain MAPb(Br$_{0.70}$I$_{0.30}$)$_3$). The mixed solutions were then spin-cast onto the quartz substrates at 1000 rpm for 10 s then 4000 rpm for 30 s. When 8 s passed after the spin turned 4000 rpm, 0.2 mL of anhydrous chlorobenzene was dropped on the substrate. The films were transferred on a hotplate of 100 °C immediately, and thermally annealed for 10 min, again in a nitrogen-filled glove box. The temperature of the heat diffuser was verified with a thermocouple. This spin-coating procedure was used for all heterostructures except that of **Figure S13** (see discussion of this figure below). The above-described preparation yielded 17% solar cell PCE for MAPbI$_3$ (see **Figure S1**).

Solar cell device fabrication and characterization (Figure S1)

Quartz substrates were cleaned and plasma-treated as described above. All procedures were performed in a nitrogen-filled glove box. A 2 mg/mL solution of PTAA in chlorobenzene was spin-cast on the substrates at 6000 rpm. The DMF solution containing MAPbI$_3$ precursors was then spin-cast as described above. A solution for the electron transport layer (30 mg/mL PCBM in chlorobenzene) was spin-cast on the MAPbI$_3$ layer at 1000 rpm. 0.02 wt.% PEIE in isopropyl alcohol was then spin-cast at 6000 rpm. The devices were finally capped with Ag (80 nm) by vacuum deposition. The *J–V* characteristics were measured at 1

sun illumination (AM 1.5G, 100mW/cm^2) in a N$_2$-filled glovebox with a solar simulator equipped with a Xenon lamp (Newport), a Keithley 2602 Source Meter and a calibrated silicon reference cell (**Figure S1**). The voltage was ramped from 1.50 V to –0.50 V then back to 1.50 V with 0.01 V step and 0.03 s delay time. The power conversion efficiency (PCE) was calculated with the following equation: PCE (%) = 100 × V_{OC} × J_{SC} × FF / P_{inc} from the open circuit voltage, V_{OC}, the short circuit current, J_{SC}, the fill factor FF and the incident powder P_{inc}.

Spin-casting of MAPb(Br$_x$I$_{1-x}$)$_3$ thin films for lattice parameter calibration curve (Figure S5c)

The procedure was identical to that described immediately above, with the following differences. PbI$_2$ and CH$_3$NH$_3$I were dissolved in DMF to make an 0.55 M solution (same procedure for PbBr$_2$ and CH$_3$NH$_3$Br), and the mixtures were stirred for >1 h at 60 °C in a nitrogen-filled glove box. The spin procedure was 2000 rpm for 1 min, with no antisolvent used. The films were annealed at 70 °C (verified with a thermocouple) for 5 min.

Fabrication of PDMS mask for heterostructures

Polydimethylsiloxane (PDMS) was fabricated by pouring 0.5 g of Sylgard 184 silicone elastomer base into an aluminum boat and adding 0.12 g of curing agent. The base and curing agent were stirred using a disposable plastic spatula until visible formation of many bubbles. The boat was then set on a flat surface, to ensure even spreading. After the last bubble disappeared, the cup was placed on a hot plate at 53 °C (as determined by thermocouple) for 10 min. The PDMS was poked with a needle to ensure no liquid remained and cut with a razor blade for use as a mask. The top surface (exposed to air) of the PDMS was contacted with the perovskite, as it was flatter than the bottom surface (that had been in contact with the bottom of the boat). Care was taken not to press the PDMS layer onto the perovskite, as this led to partial removal of the perovskite by the PDMS.

Vapor substitution to fabricate heterostructures

Briefly, a previously-reported vapor substitution setup was reproduced, with the following differences. [1] All nitrogen gas lines were purged for 5 min. 1.25 mL of liquid bromine was poured into a 50mL round-bottomed flask and allowed to equilibrate for ~ 2 min. The bromine gas stream was combined with a second nitrogen stream, leading to a second 50mL round-bottomed flask (the sample chamber). The masked thin films were dropped into the chamber (Br$_2$ concentration ≈ 0.48 atm) and kept there for ~1 min. The PDMS mask was then carefully removed from the heterostructure.

Interdiffusion experiments

Prior to heating, we spin-coated a thin layer of polystyrene on top of the heterostructures, both to prevent desorption of methylammonium, enabling lengthy and high-temperature experiments, and to minimize diffusion along the perovskite surface. The heterostructures were heated for extended times (up to 360 min.) on a hot plate with a heat diffuser in a nitrogen-filled glove box. The heat diffuser was encased in aluminum foil to ensure that the

samples were kept in the dark, as light may affect halide transport. At particular time points, the heterostructures were transported from the hot plate (in the glove box) to the optical microscope for analysis. The time from hot plate to microscope was < 5 min. The heterostructures were then transported back to the glove box, and put on the hot plate again. The total time off the hot plate at each time point was < 10 min.

Characterization and Equipment

Optical microscopy images were acquired using an Olympus BH-2 microscope in transmission mode. X-Ray Diffraction patterns were acquired using an Empyrean Powder Diffractometer with a step size of 0.01313^o, with a Cu-Kα source, operating with an accelerating voltage of 45 kV and beam current of 40 mA, with samples rotated at 4 revolutions/min to improve signal-to-noise ratios. UV-Vis spectra were acquired using a Shimadzu UV3600 UV-Nir-NIR Spectrometer with a step of 1 nm, in ambient conditions. Scanning Electron Microscopy/Energy Dispersive X-Ray data was acquired using both an FEI XL30 Sirion FEG SEM and a ThermoFischer Apreo C LoVac FEG SEM with EDX detectors. 10keV was used in both SEMs so as to be able to detect iodine with an adequate signal-to-noise ratio via EDX. Confocal microscopy was performed on a Leica SP8 Laser Scanning Confocal microscope, with a laser excitation wavelength of 458 nm. Time-resolved PL were collected using an inverted microscope (Nikon Eclipse Ti-U) at 20x magnification. Samples were continuously excited by a 405nm laser (Thorlabs S1FC405) through a 20x objective, with power density $\approx$ 160 mW/cm^2 at the level of the sample, and PL was continuously collected with 1 s integration times through the same objective and was passed through the entrance slit of an imaging spectrometer (Princeton Instruments IsoPlane), spectrally separated by a 150 lines/mm grating, and collected with a CCD array (Princeton Instruments Pixis). A standard 405nm PL filter set (Semrock) was used for all PL measurements to remove excitation wavelengths from the collected signal.

Image integration to obtain interface profiles

To obtain interface profiles, optical and EDX microscopy images were integrated using FIJI/ImageJ software. The optical images were converted to grayscale by taking the average values of the red, green and blue pixels, giving each pixel equal weight. The entire image area was then selected and then collapsed (integrated) to a line using the "plot profile" function. This methodology was used (rather than obtaining simple linecuts of the images) in order to improve signal-to-noise ratios, which was particularly important for EDX-obtained interface profiles. Compositional verification of the optically-obtained interface profiles was performed using EDX, with MAPbBr$_3$ and MAPbI$_3$ baseline compositional verifications performed in regions far from the interface.
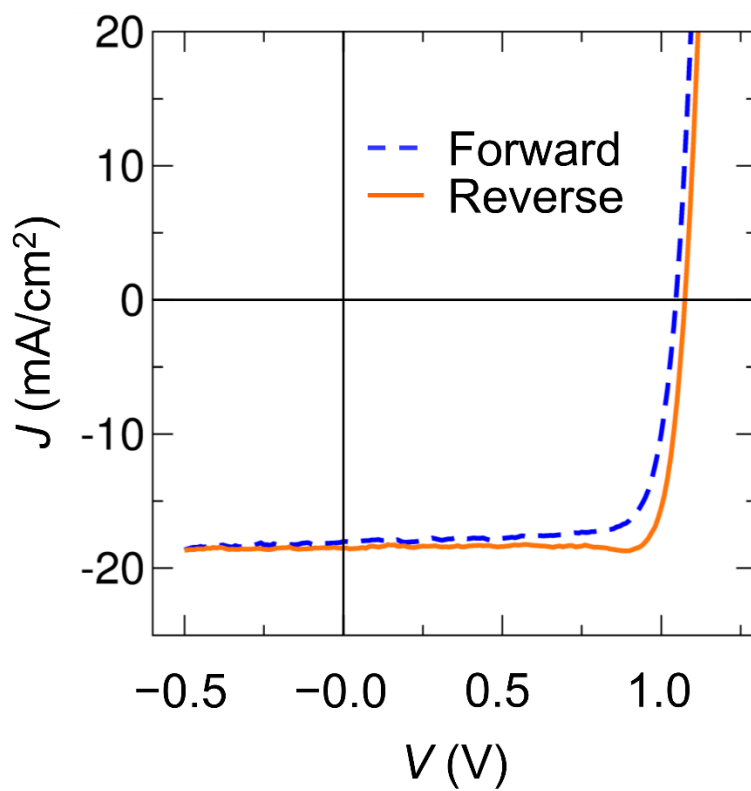
Figure S1. Current-Voltage (*J-V*) curve for a solar cell made from $MAPbI_3$ with an ITO/PTAA/MAPbI3/PEIE/Ag device structure with V_{oc}=1.07 V, J_{sc} = 18.5 mA/cm², FF=0.86 and power conversion efficiency of 17.6% under 1 Sun simulated solar illumination, in forward and reverse bias.
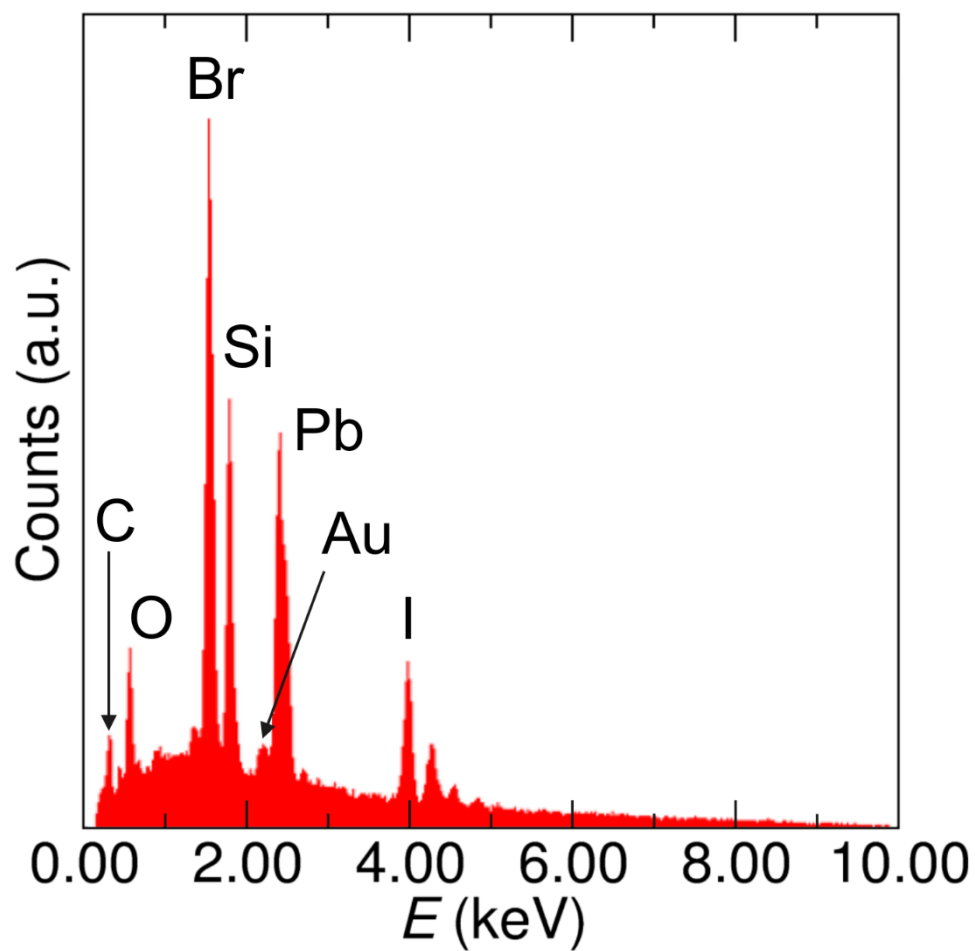
Figure S2. EDX spectrum of the gold-coated x_{Br} =0|1 heterostructure in **Figure 3a** (fabricated on a quartz substrate).
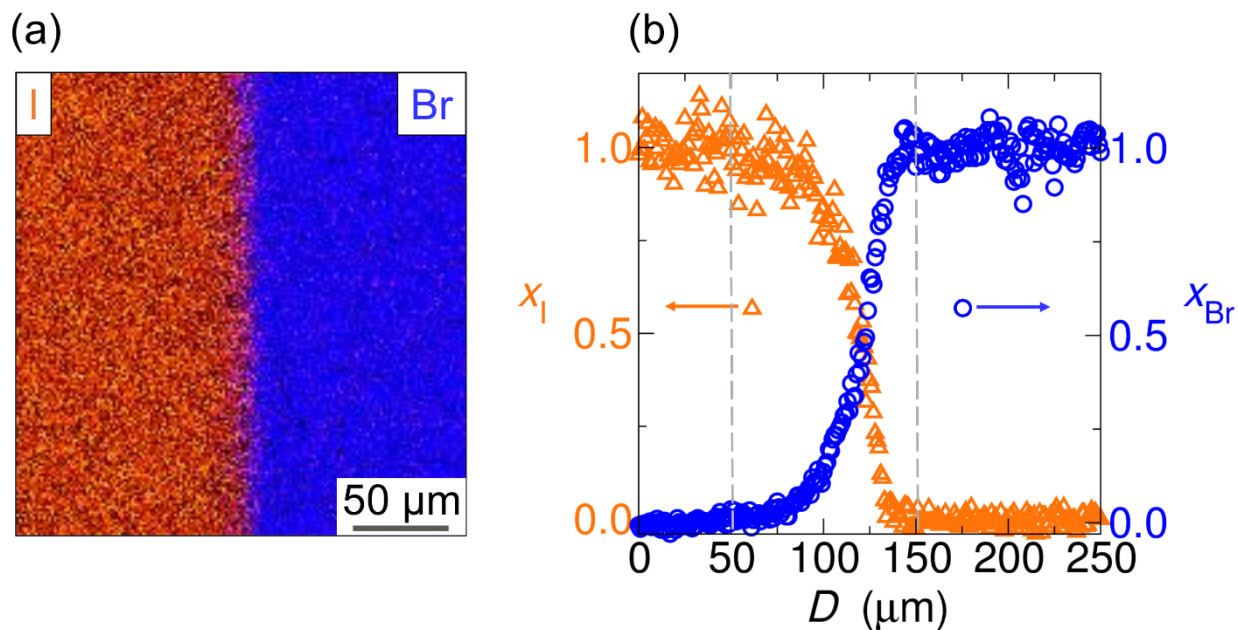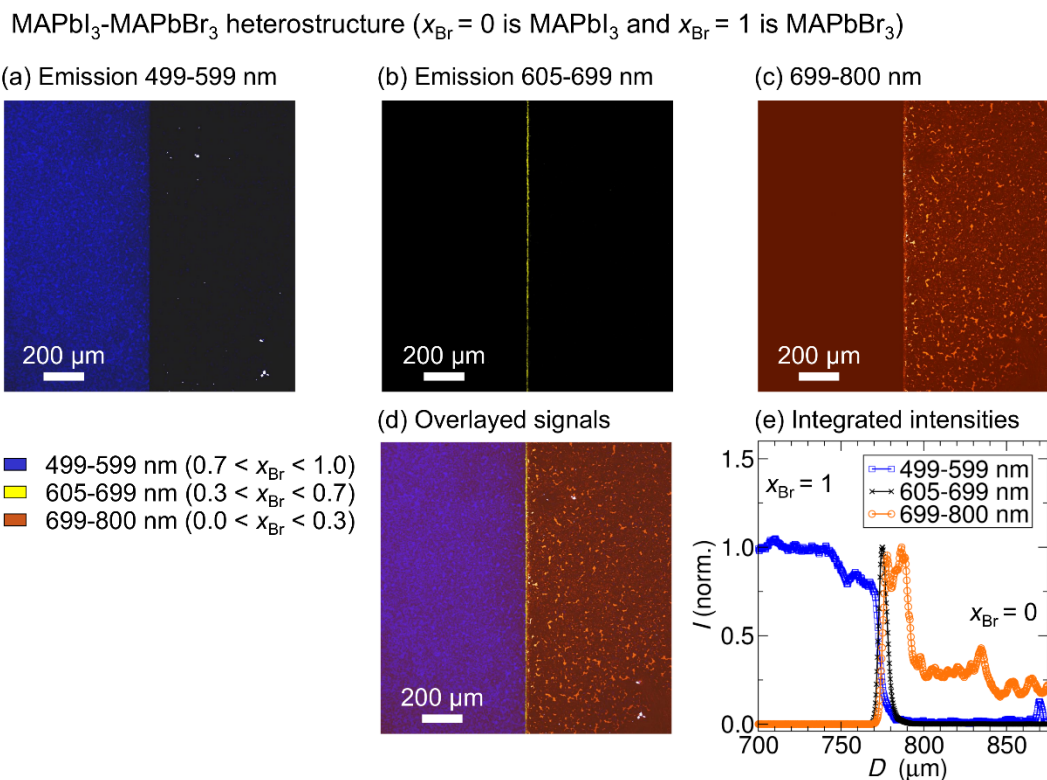
Figure S3. Overlayed EDX iodine and bromine maps (a) and integrated EDX interface profiles (b) of the x_{Br} =0|1 heterostructure shown in **Figure 3a** where x_{Br} and x_I represent the halide fractions of Br and I respectively.

The x_{Br} = 0, x_{Br}=1, x_I = 0, and x_I = 1 compositions far from the interface were assigned by taking EDX baseline compositions were obtained far from the interface (data not shown) to confirm lack of iodine in MAPbBr$_3$ regions and lack of bromine in MAPbI$_3$ regions. Compositions far from the interface were separately confirmed via XRD and UV-Vis (**Figures 2** and **S6**). The halide interface profiles of **Figure S3** are thus compositionally representative.

MAPbI$_3$ Increasing x_{Br}

(a) Perovskite

SiO$_2$

20 μm

(b) Iodine EDX map

20 μm
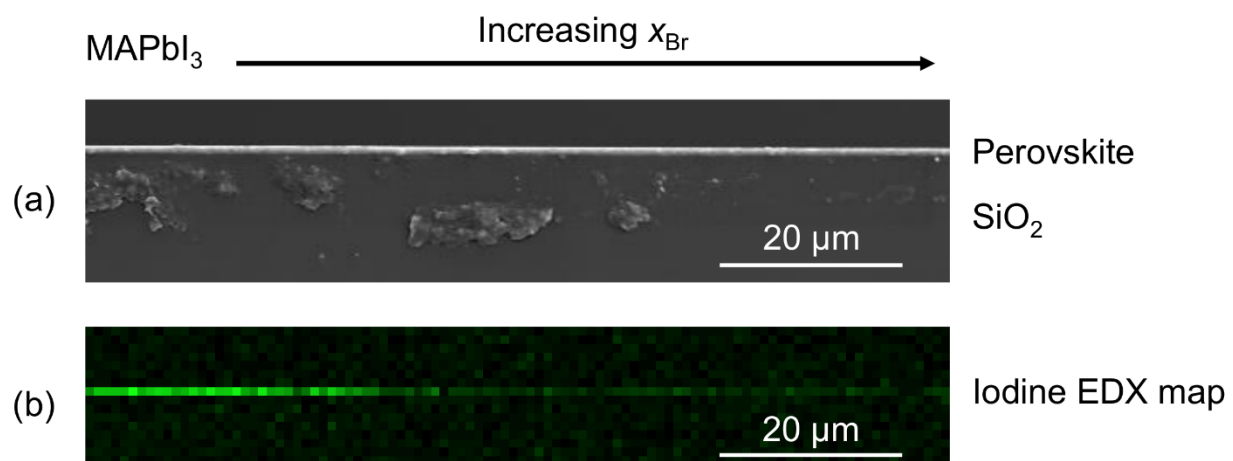
Figure S4. (a) Cross-sectional SEM and (b) corresponding iodine EDX map of a MAPbI$_3$-MAPbBr$_3$ heterostructure before heating.
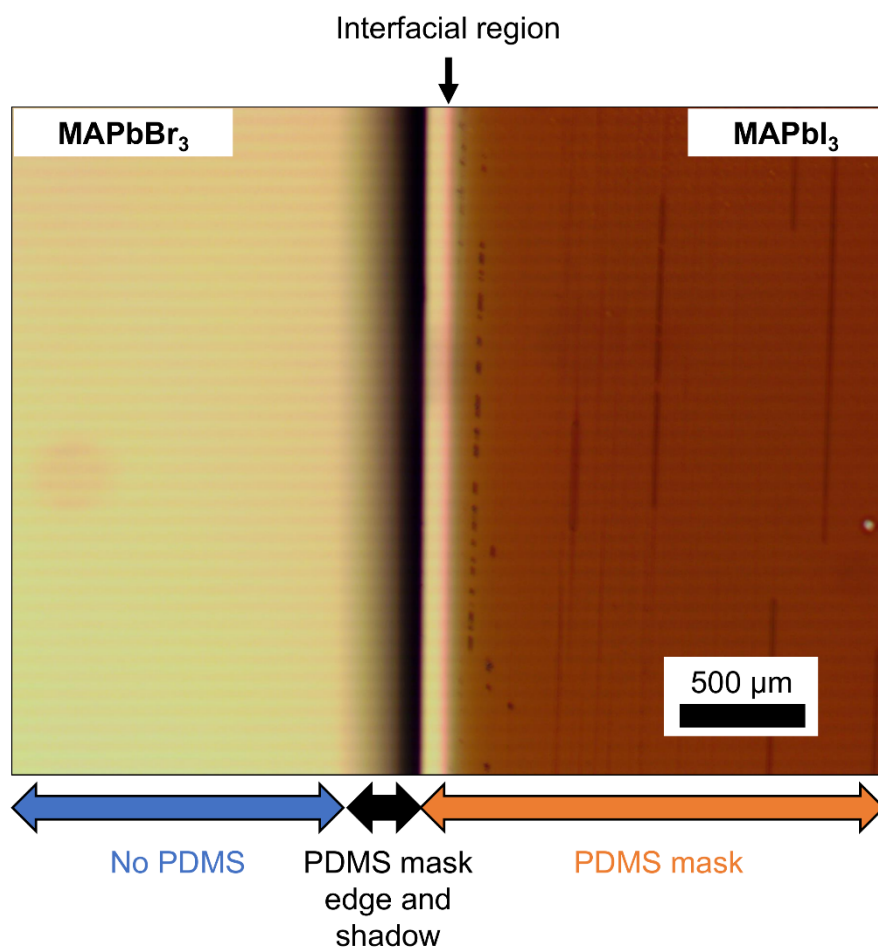
MAPbI$_3$-MAPbBr$_3$ heterostructure (x_{Br} = 0 is MAPbI$_3$ and x_{Br} = 1 is MAPbBr$_3$)

(a) Emission 499-599 nm (b) Emission 605-699 nm (c) 699-800 nm

499-599 nm (0.7 < x_{Br} < 1.0)
605-699 nm (0.3 < x_{Br} < 0.7)
699-800 nm (0.0 < x_{Br} < 0.3)

(d) Overlayed signals (e) Integrated intensities

Figure S5. Confocal microscopy image of an x_{Br} = 0|1 heterostructure, for an excitation wavelength of 458 nm. Images (a)-(d) represent emission between (a) 499-599 nm, (b) 605-699 nm, (c) 699-800 nm and (d) is an overlay of these emission signals. x_{Br} composition assignments were made using reference [2]. (e) Represents the integrated intensities of each emission (normalized).

Emission between 499 nm and 599 nm includes emission from x_{Br} = 1 (at ~540 nm) as well as from some Br-rich phases (0.7 < x_{Br} < 1.0), based on previously-published work.[2] The 699-800 nm emission channel covers x_{Br} = 0 (at ~780 nm) as well as some I-rich phases (0.0 < x_{Br} < 0.3). Correspondingly, the 605-699 nm emission channel covers intermediate mixed-halide phases not included in the other two emission channels (0.3 < x_{Br} < 0.7). Observation of 605-699 nm emission indicates emission from mixed-halide compositions (0.3 < x_{Br} < 0.7) under light exposure at 458 nm, which is expected given the short exposure times in scanning confocal microscopy (~ microsecond). This approximate composition assignment is in agreement with composition assignment from optical microscopy and EDX (**Figures 4e** and **6**), as emission from the 605-699 nm channel spans a width of ≈ 10 μm, corresponding to the interface width for 0.3 < x_{Br} < 0.7. Given the large width of emission peaks from MAPb(Br$_x$I$_{1-x}$)$_3$, [2,3] the observed overlap between channels is not surprising. We therefore relied on EDX for exact composition determination (**Figures 4** and **S3**). The decrease in intensity near 800 μm in the 699-800 nm emission channel (0.0 < x_{Br} < 0.3) likely stems from emission being cut off at 800 nm in this channel, which cuts off some of the MAPbI$_3$ emission (emission center wavelength 775 nm)[2] and other low x_{Br} emission.
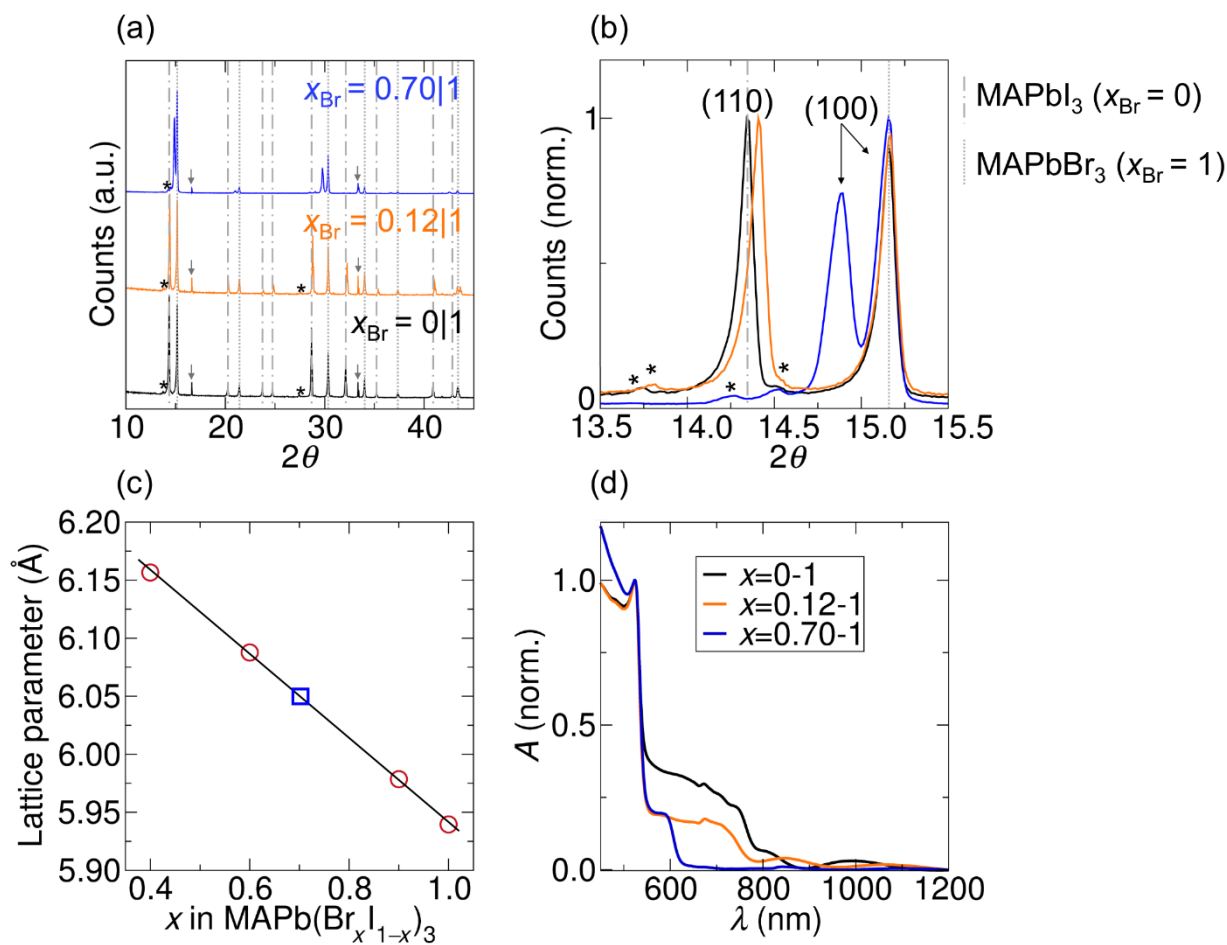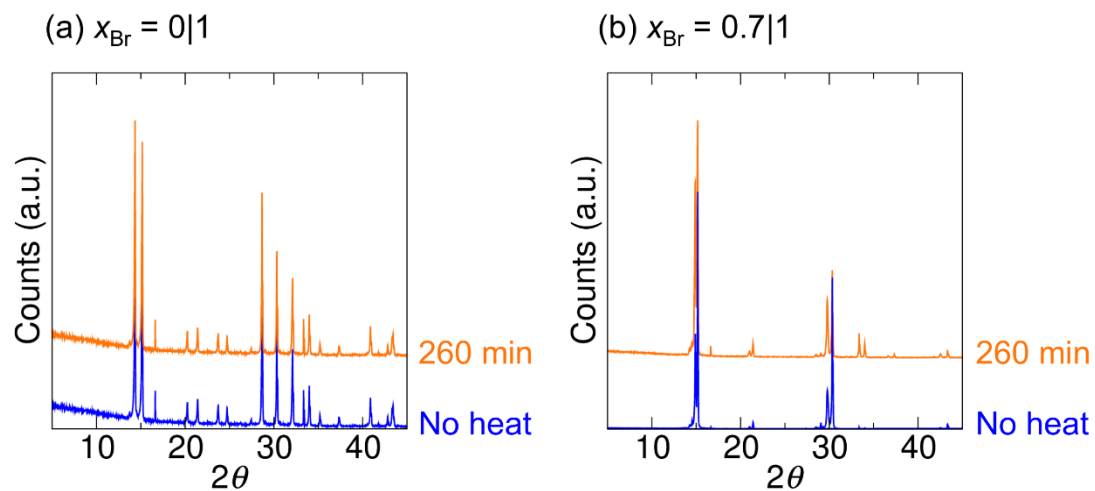
Figure S6. (a, b) XRD patterns of x_{Br} = 0.7|1 and x_{Br} = 0.12|1 heterostructures after 260 min of heating, with for comparison x_{Br} = 0|1 before heating. The gray lines are a guide to the eye, with large dashes indicating MAPbI$_3$ (x_{Br} = 0) peaks and the small dashes indicating MAPbBr$_3$ (x_{Br} = 1) peaks. The downwards gray arrows in (a) designate peaks from the quartz substrate and the * indicate extra (110) and (100) peaks arising from Tungsten (1.4764 Å) and CuKβ (1.3926 Å) radiation contamination in the X-ray source. (c) Calibration curve made from the (100) XRD peaks of spin-coated MAPb(Br$_x$I$_{1-x}$)$_3$ thin films to verify the XRD x_{Br} = 0.70 (blue box) and x_{Br} = 1 assignments. (d) UV-Vis spectra of x_{Br} = 0.70|1 and x_{Br} = 0.12|1 heterostructures after heating to 100°C for 260 min and of x_{Br} = 0|1 before heating.

For all XRD pattern analyses, a z-height correction was applied to match the x_{Br} = 1 lattice parameter with the known lattice parameter of MAPbBr$_3$ from the reported CIF file. [4] The calibration curve in (c) matches that of previous works to within the step size of our instrument (2θ = 0.01313°). [2,5] The band onsets for MAPbI$_3$ and MAPbBr$_3$ are visible at ~795 nm and ~540 nm respectively, as well as the onsets for x_{Br} = 0.12 at ~775 nm and for x_{Br} = 0.7 at ~625 nm. Interference fringes become apparent at longer wavelengths.
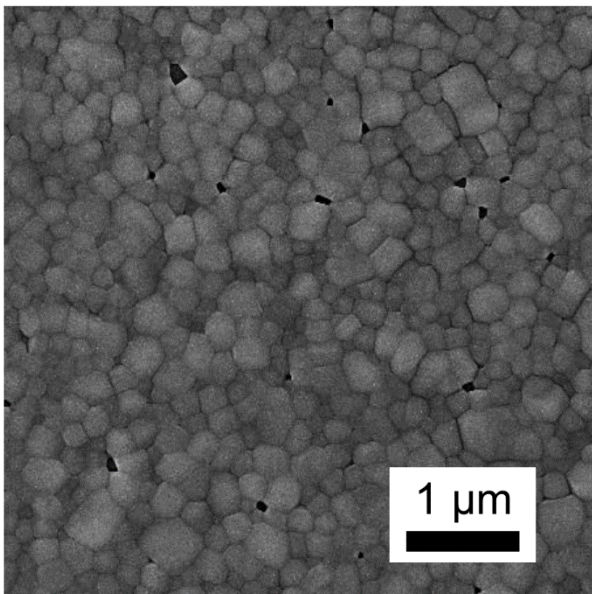
Figure S7. Optical microscopy image of an MAPbBr$_3$-MAPbI$_3$ heterostructure with the PDMS mask still on the MAPbI$_3$ side.

Figure S7 shows a MAPbBr$_3$-MAPbI$_3$ heterostructure, with the PDMS mask still on it. The thick black stripe indicates the location of the edge of the $\approx$ 450 µm mask, as well as the mask's shadow. The location of the PDMS mask to the left of the interfacial region indicates that Br$_2$ bled under the mask. The coincidence of the locations of the PDMS mask and of the optical artifact in **Figures 4/6** strongly suggests that the artifact arises due to residual PDMS on the film.
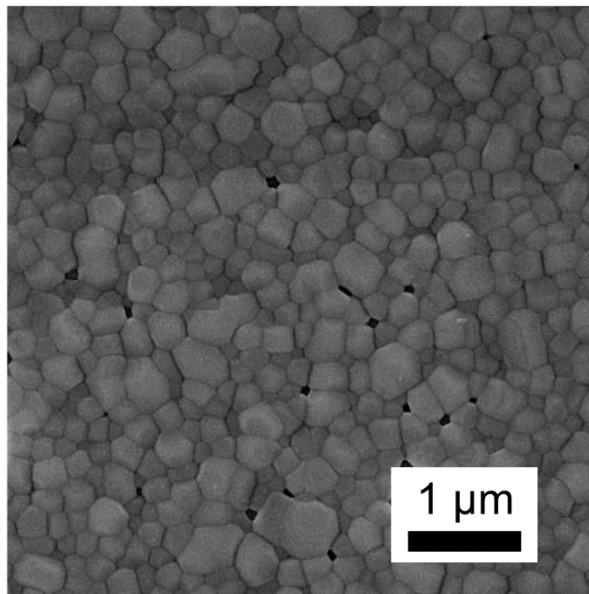
Figure S8. XRD patterns of x_{Br} = 0|1 (a) and x_{Br} = 0.7|1 (b) before and after 260 min of heating, showing no change, and therefore little degradation. Notably, a PbI_2 peak at $\approx$ 12° does not appear after heating.

(a) No heat

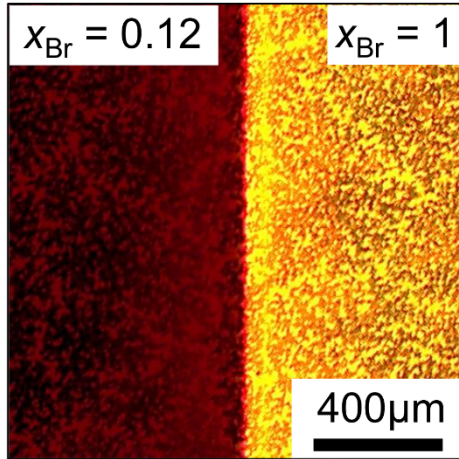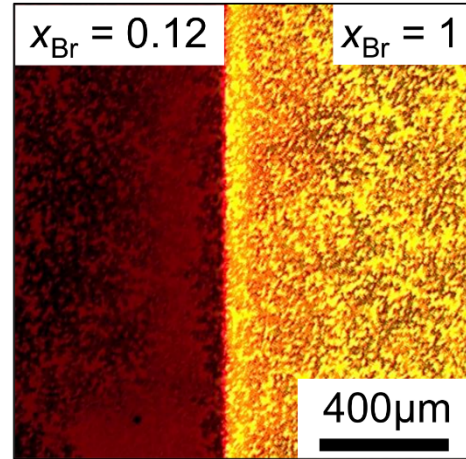**(b) 240 min at 70°C**

1 µm

1 µm

Figure S9. Top-view SEM of two halves of the same fully-brominated film (a) without heating and (b) after heating at 70°C for 240 min.

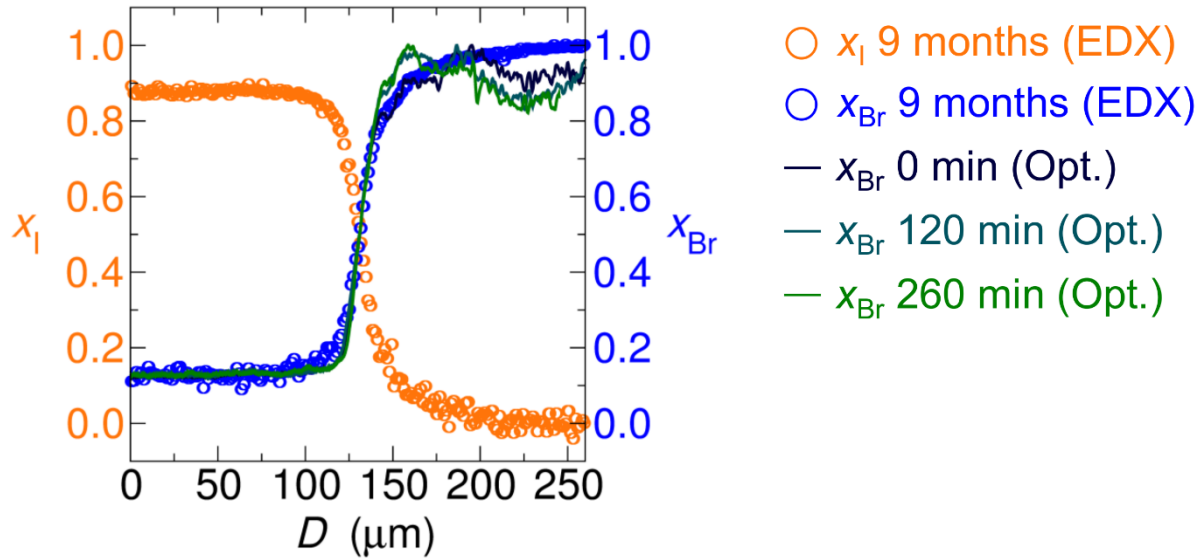**(a) 0 min at 100°C**

$x_{Br} = 0.12$ $x_{Br} = 1$

400µm

(b) 260 min at 100°C

$x_{Br} = 0.12$ $x_{Br} = 1$

400µm

(c) Interface profiles

- ○ x_I 9 months (EDX)
- ○ x_{Br} 9 months (EDX)
- — x_{Br} 0 min (Opt.)
- — x_{Br} 120 min (Opt.)
- — x_{Br} 260 min (Opt.)

Figure S10. Optical microscopy images of the same x_{Br}=0.12|1 heterostructure before (a) and after (b) heating at 100°C for 260 min, obtained via illumination with white light. (c) Interface profiles of the heterostructure after 0 min, 137 min and 260 min of heating at 100°C, and after storage at room temperature for 9 months. The deviations between optical microscopy and EDX at high x_{Br} are interpreted as noise.
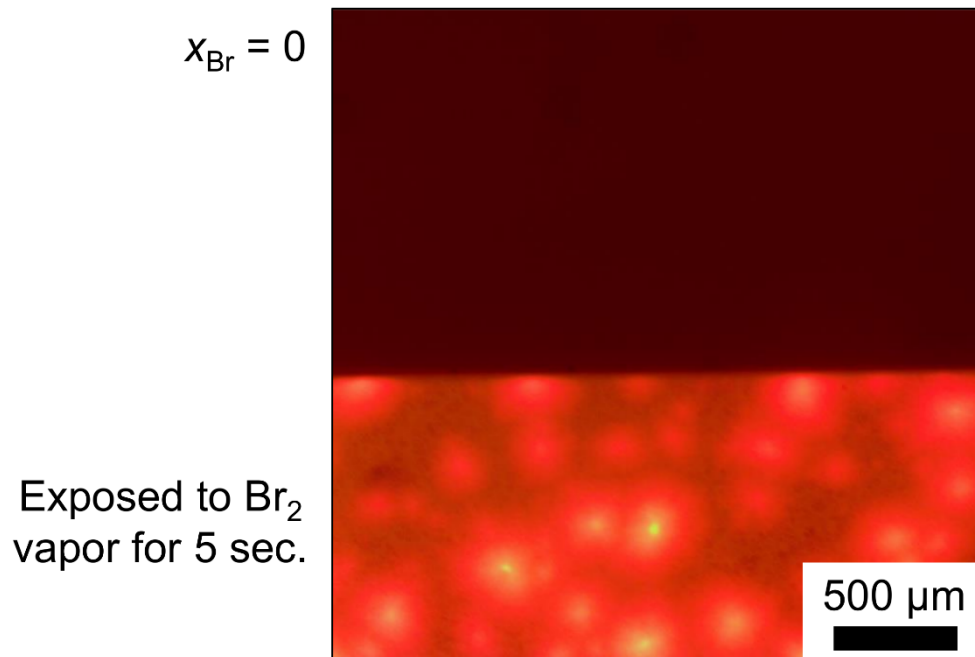
Figure S11. Optical microscope image of a MAPbI$_3$ film (x_{Br} = 0) exposed on the bottom half to Br$_2$ vapor in an N$_2$ environment for 5 sec, demonstrating the unevenness of the bromination reaction.
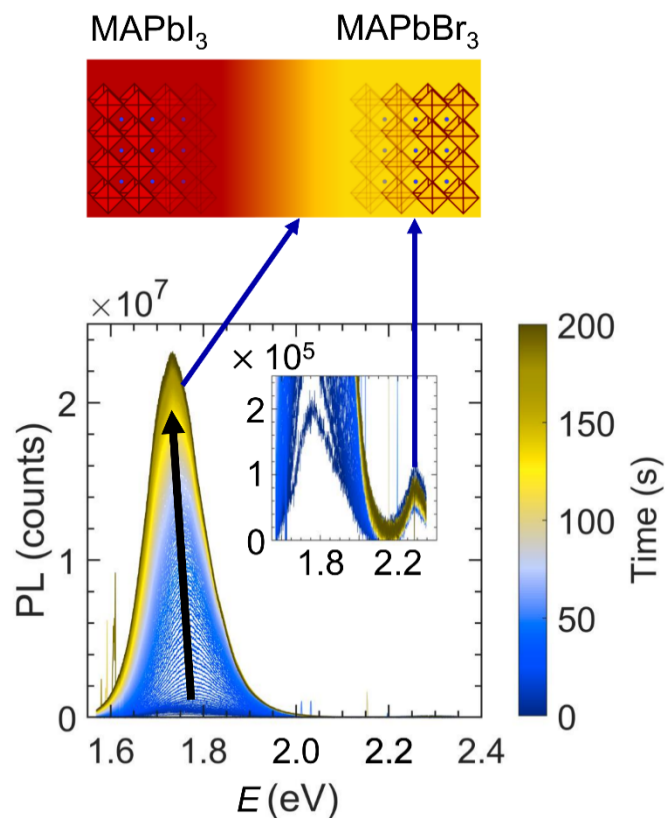
Figure S12. Time-dependent photoluminescence spectra of localized regions (the interfacial and MAPbBr$_3$ regions) of an x_{Br} = 0|1 heterostructure under 405 nm excitation (continuous collections with 1 s integration times), with a power density ≈ 14 mW/cm^2 at the level of the sample.

The gradually increasing and red-shifting peak at ≈ 1.7 eV indicates light-induced phase separation in the mixed-halide interfacial region. [2] The gradual red-shift of the peak at ≈ 1.7 eV indicates formation of I-rich regions that increase in iodine content. The inset shows photoluminescence peaks at low intensity, with constant MAPbBr$_3$ emission visible at 2.3 eV.
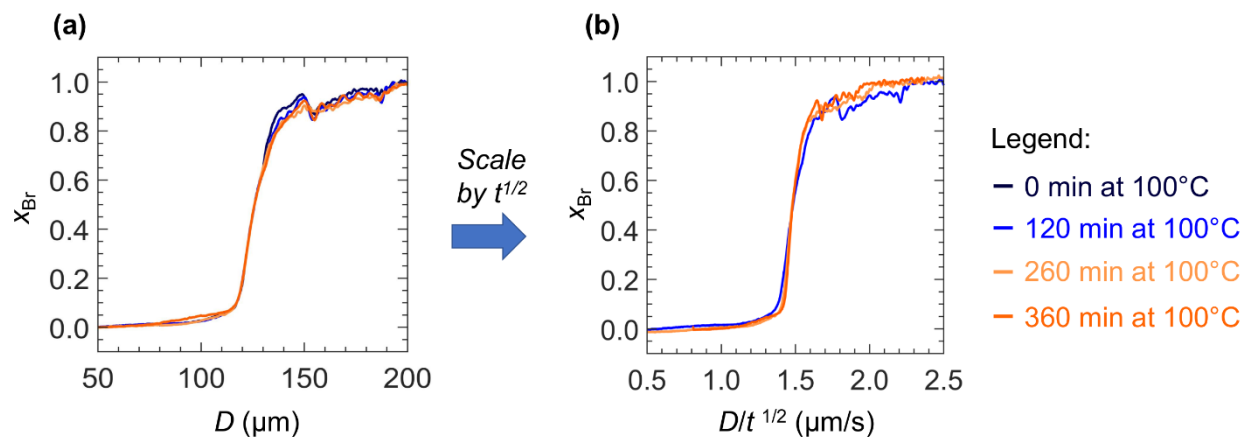
Figure S13. Bromide fraction x_{Br} vs. distance (a), which was then normalized by the square root of time $t^{1/2}$ (i.e. the Boltzmann transformation) (b) for the optical microscopy-obtained traces of the x_{Br} = 0|1 heterostructure in **Figure 6**.

Dividing distance axis of the interface profiles by $t^{1/2}$, the square root of the time (120 min, 260 min, or 360 min at 100°C), resulted in lack of interface profile overlap. This confirmed that Fick's second law cannot be used to determine D_i, assuming a solid solution regime.

Section S9 – Simulations of Fick's Second Law

To approximate D_i, we used the error function solution for a diffusion couple (binary system) based on Fick's second law, for a solid solution regime: [6,7]

$$c(d, t) = \frac{c_R + c_L}{2} + \frac{c_R - c_L}{2} \, erf\left(\frac{d}{\sqrt{4D_i t}}\right) \tag{1}$$

Where $c(d, t)$ is the concentration of a species having diffused a distance d after heating for a time t, c_R and c_L are the concentrations of that same species very far away from the interface (at infinity) on the right and left sides of the interface respectively, and D_i is the interdiffusion coefficient, which in this expression is constant with respect to composition.

Initial and boundary conditions

Equation (1) can be used as an approximation for concentration-dependent interdiffusion provided that the following boundary and initial conditions hold true: c_R and c_L are uniform compositions extending to quasi-infinity, and the initial shape of the diffusion couple is a step-wise function. [6-8] Because the as-fabricated heterostructures exhibited a wide interface rather than a step-wise shape, we made the following assumption. The initial (fictional) form of the interface profiles was a step function. After a time t_0, halides (fictionally) interdiffused, forming the wide interface that was initially observed upon fabrication (**Figures 4**, **6**, **7** and **S10**). For each D_i (10^{-10} - 10^{-13} cm^2/s), t_0 was adjusted, so that the simulated error function would overlap as best as possible with the interfacial profile of the $x_{Br} = 0|1$ heterostructure upon fabrication (0 min of heating). Times heated (360 min) or stored at room temperature (8 months) were subsequently added to t_0 (i.e. $t + t_0$) to simulate the error function. For all $x_{Br} = 0|1$ simulations, $c_R = 1$ (MAPbBr$_3$) and $c_L = 0$ (MAPbI$_3$), and for all $x_{Br} = 0.70|1$ simulations, $c_R = 1$ (MAPbBr$_3$) and $c_L = 0.7$. Below is a summary of the simulation parameters used for equation (1).
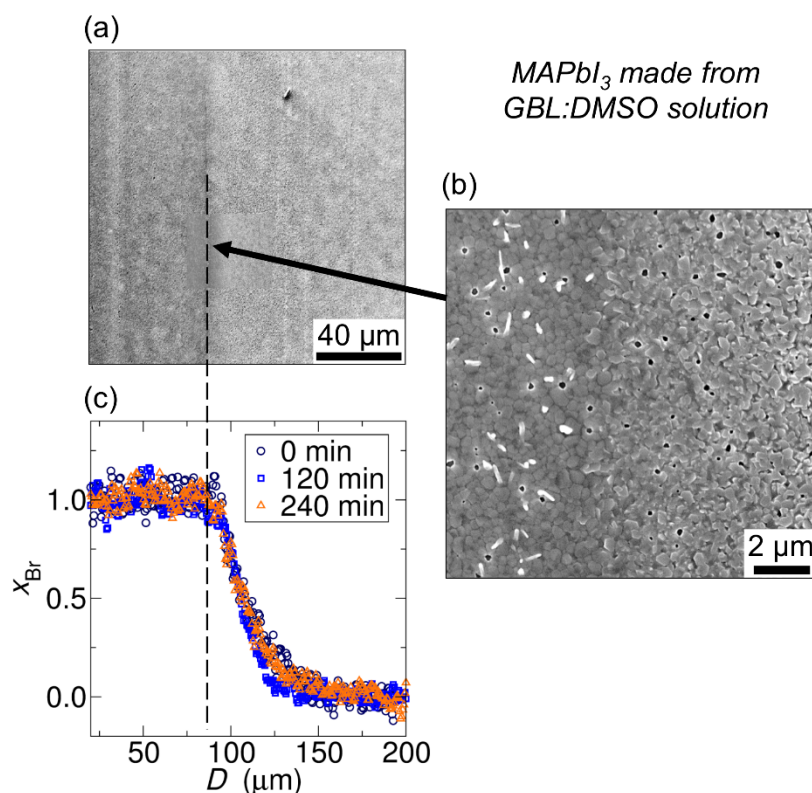
Table S1. Parameters for simulations of Fick's second law (equation 1)

Figure	D_i (cm^2/s)	t_0 (s)
4, S12 (100°C for 0 min and 260 / 360 min)	10^{-10}	4000
	10^{-11}	40000
	10^{-12}	400000
	10^{-13}	4000000
5 (Room temp. for 8 months)	10^{-10}	6500
	10^{-11}	65000
	10^{-12}	650000
	10^{-13}	6500000
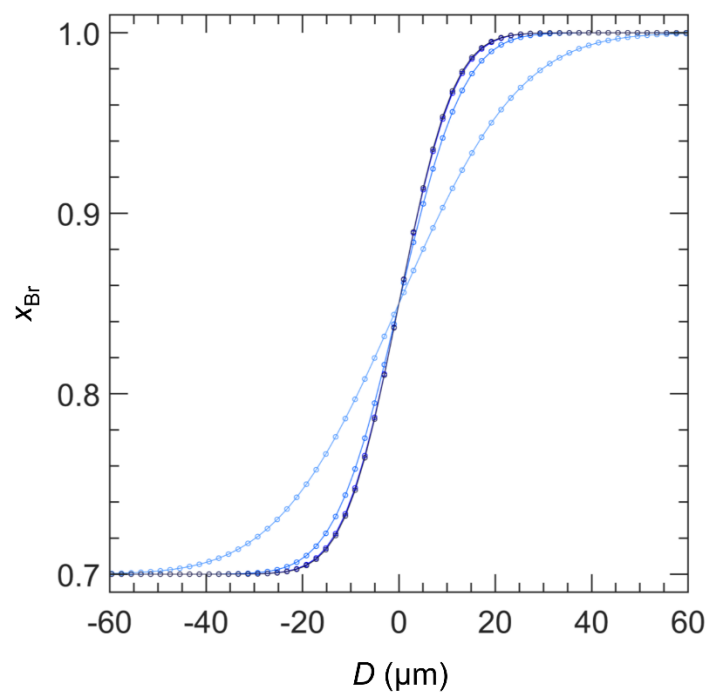
Figure S14. Calculated interfacial profiles for x_{Br} =0.70|1, for 0 min and 260 min of heating, using the parameters of **Table S1.**

Figure S15. SEM/EDX study of an x_{Br} = 0|1 heterostructure made from poorer-quality MAPbI$_3$ films. (a) Plan view SEM image of the x_{Br} = 0|1 heterostructure after heating at 70 °C for 120 min. (b) Higher-magnification image of the section of the interface indicated by the black arrow. (c) EDX-determined interface profiles of the heterostructure in (a) after heating at 70 °C for 0 min, 120 min, and 240 min, where the profiles were determined by fraction of halide x that is Br. The vertical dashed line indicates correspondence between the SEM image and the Br composition profile.

We examined whether changes in the interface profile were affected by the spin-coating process for MAPbI$_3$. The heterostructure in **Figure S15** was fabricated as described above in all ways except the spin-casting of x_{Br} = 0 perovskite. Here, PbI$_2$ and CH$_3$NH$_3$I were dissolved in 300 μL DMSO and 700 μL γ-butyl lactone (GBL) to make a 1M solution, and the mixture was stirred for >1 h at 60°C in a nitrogen-filled glove box. The solution was then spin-cast onto quartz substrates using a two-step procedure: 1000 rpm for 10 s, with a 200 rpm/s acceleration then 5000 rpm for 20 s with a 1000 rpm/s acceleration. A few drops of chlorobenzene were dispensed onto the spinning substrate ~5 s prior to the end of the spin-coating procedure to aid crystallization. The thin films were then annealed on a hot plate with a heat diffuser at 34°C for 2 min, at 40°C for 2 min, at 50°C for 2 min, and at 70°C for 10 min (temperatures were verified with a thermocouple) again in a nitrogen-filled glove box. These films yielded 8% solar cell PCE (data not shown).

Consistent with our other heterostructure analyses, we observed little change in the interface profiles after heating (**Figure S15a** and **Figure S15c**). Here, the heterostructure was heated to 70°C rather than to 100°C. No interface profile flattening was observed via EDX after 240 min of heating. Because the linewidth of our EDX traces was ≈ 3 μm, we took this to be the maximum possible distance travelled by halides after 240 min. Using equation (1), we then obtained an interdiffusion coefficient $D_i \leq 10^{-13}$ cm^2/s at 70°C.
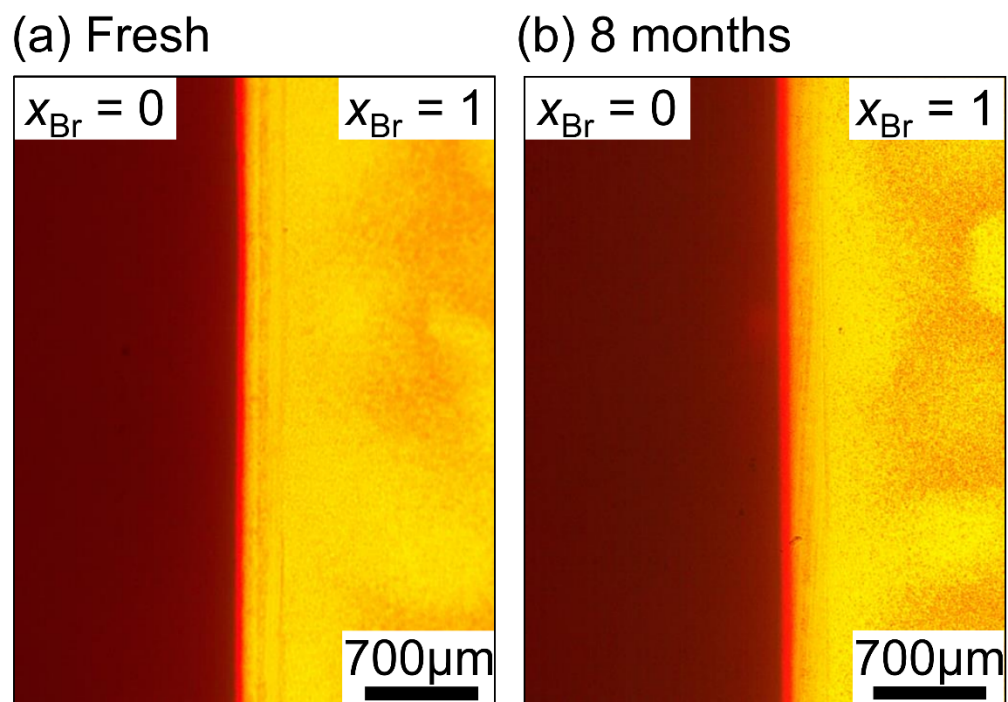
Figure S16. Optical microscopy images of the x_{Br} = 0|1 heterostructure from **Figure 8**, before (a) and after (b) storage for 8 months. The strong retention of initial color indicates substantial retention of perovskite phases.

References

(1)   Solis-Ibarra, D.; Smith, I. C.; Karunadasa, H. I. Post-Synthetic Halide Conversion and Selective Halogen Capture in Hybrid Perovskites. *Chem. Sci.* **2015**, *6* (7), 4054 - 4059.

(2)   Hoke, E. T.; Slotcavage, D. J.; Dohner, E. R.; Bowring, A. R.; Karunadasa, H. I.; Mcgehee, M. D. Reversible Photo-Induced Trap Formation in Mixed- Halide Hybrid Perovskites for Photovoltaics. *Chem. Sci.* **2015**, *6* (613).

(3)   Barker, A. J.; Sadhanala, A.; Deschler, F.; Gandini, M.; Senanayak, S. P.; Pearce, P. M.; Mosconi, E.; Pearson, A. J.; Wu, Y.; Ram Srimath Kandada, A.; Leijtens, T; De Angelis, F.; Dutton, S. E.; Petrozza, A.; Friend, R. H. Defect-Assisted Photoinduced Halide Segregation in Mixed-Halide Perovskite Thin Films. *ACS Energy Lett.* **2017**, *2*, 1416 - 1424.

(4)   Jaffe, A.; Lin, Y.; Beavers, C. M.; Voss, J.; Mao, W. L.; Karunadasa, H. I. High-Pressure Single-Crystal Structures of 3D Lead-Halide Hybrid Perovskites and Pressure Effects on Their Electronic and Optical Properties. *ACS Cent. Sci.* **2016**, *2*, 201 - 209.

(5)   Noh, J. H.; Im, S. H.; Heo, J. H.; Mandal, T. N.; Seok, S. Il. Chemical Management for Colorful, Efficient, and Stable Inorganic - Organic Hybrid Nanostructured Solar Cells. *Nano Lett.* **2013**, *13*, 1764 - 1769.

(6)   Balluffi, R. W.; Allen, S. J.; Carter, C. W. *Kinetics of Materials*; John Wiley & Sons: Hoboken, NJ, 2005.

(7)   Shewmon, P. G. *Diffusion in Solids.*; Springer, 2016; Vol. 36.

(8)   Crank, J. *The Mathematics of Diffusion*, 2nd Ed.; Oxford University Press: Uxbridge, 1975.